

# THE DYNAMICS OF RADIATIVE SHOCK WAVES: LINEAR AND NONLINEAR EVOLUTION

A. Mignone<sup>1,2,3</sup>

## ABSTRACT

The stability properties of one-dimensional radiative shocks with a power-law cooling function of the form  $\Lambda \propto \rho^2 T^\alpha$  are the main subject of this work. The linear analysis originally presented by Chevalier & Imamura, is thoroughly reviewed for several values of the cooling index  $\alpha$  and higher overtone modes. Consistently with previous results, it is shown that the spectrum of the linear operator consists in a series of modes with increasing oscillation frequency. For each mode a critical value of the cooling index,  $\alpha_c$ , can be defined so that modes with  $\alpha < \alpha_c$  are unstable, while modes with  $\alpha > \alpha_c$  are stable. The perturbative analysis is complemented by several numerical simulations to follow the time-dependent evolution of the system for different values of  $\alpha$ . Particular attention is given to the comparison between numerical and analytical results (during the early phases of the evolution) and to the role played by different boundary conditions. It is shown that an appropriate treatment of the lower boundary yields results that closely follow the predicted linear behavior. During the nonlinear regime, the shock oscillations saturate at a finite amplitude and tend to a quasi-periodic cycle. The modes of oscillations during this phase do not necessarily coincide with those predicted by linear theory, but may be accounted for by mode-mode coupling.

*Subject headings:* hydrodynamics - instabilities - methods: numerical - shock waves - stars: binaries: close

## 1. INTRODUCTION

Radiative shock waves are believed to play a key role in a variety of different astrophysical environments, including magnetic cataclysmic variables (Wu 2000; Cropper 1990), jets from young stellar objects (Hartigan et al. 1994), magnetospheric accretion in T-Tauri stars (Calvet & Gullbring 1998), colliding stellar winds (Stevens et al. 1992; Antokhin et al. 2004) and supernova remnants (Kimoto & Chernoff 1997; Blondin et al. 1998; Walder & Folini 1998).

Most of the earlier theoretical investigation has been motivated by the dynamics of accreting shocks in magnetic cataclysmic variables. In these systems, a strongly magnetized white dwarf ( $10^6 \lesssim B \lesssim 10^8$  Gauss) accretes matter directly from a late-type star without the formation of a disk. Instead, the mass transfer process is magnetically channeled and matter accumulates through a stand-off shock on a small fraction of

---

<sup>1</sup>INAF Osservatorio Astronomico di Torino, Strada dell'Osservatorio 20, 10025 Pino Torinese, Italy

<sup>2</sup>Department of Astronomy & Astrophysics, The University of Chicago, Chicago, IL 60637

<sup>3</sup>Center for Astrophysical Thermonuclear Flashes, The University of Chicago, Chicago, IL 60637

the stellar surface. At temperatures of  $10^8 \div 10^9$  K, the shock-heated plasma radiates its energy via optically thin bremsstrahlung becoming a powerful source of X-rays.

It has been shown that, under certain circumstances, the postshock flow is subject to a global thermal instability (more precisely, an overstability) caused by rapid variations of the cooling time scale with the shock speed. The instability drives the shock front to oscillate with respect to its stationary position, causing variations in the amount of radiation emitted from the postshock region. The instability mechanism has been invoked in the past to explain the optical quasi-periodic-oscillations (QPO) observed in AM Her-type systems (Larsson 1992; Middleditch et al. 1997; Wu 2000). Similarly, a relevant issue arises in questioning the validity of steady shock models with shock velocities  $v_s \gtrsim 130 \text{ km s}^{-1}$ , routinely used in interpreting emission line observations from interstellar shocks (Innes et al. 1987a,b; Gaetz et al. 1988; Sutherland et al. 2003).

The nature of the instability was first studied analytically by Chevalier & Imamura (1982, CI hereafter), who presented a linear stability analysis of planar radiative shocks with volumetric cooling rate  $\Lambda \propto \rho^2 T^\alpha$ . CI showed that the shock has multiple modes of oscillation, and the stability of a particular mode depends on the value of the cooling index  $\alpha$ . In general, higher power dependences on the temperature were shown to inhibit the growth of instability. Thus the fundamental mode was shown to become unstable for  $\alpha \lesssim 0.4$ , while the first and second harmonics are de-stabilized when  $\alpha \lesssim 0.8$ . Higher order harmonics were not considered by CI.

Perturbative studies of one-temperature flows with a power-law cooling function were afterwards considered by several authors. Imamura (1985) presented a linear stability study of radiative shocks where the cooling function had a weaker dependence on density, i.e.  $\Lambda \propto \rho T^\alpha$ . Bertschinger (1986) examined the structure of spherical radiative shocks and also considered the effects of nonradial perturbations. He showed that modes that are stable to radial perturbations may become unstable for small transverse wavenumbers. For sufficiently large wavenumbers, however, all modes are eventually stabilized.

Effects due to cyclotron emission were considered in Imamura et al. (1991), Wu et al. (1992), Wu et al. (1996). Noise driven models were proposed by Wood et al. (1992). Effects of gravity were studied by Houck & Chevalier (1992), while magnetic field effects were considered by Edelman (1989a), Edelman (1989b), Tóth & Draine (1993), and by Hujerir & Papaloizou (1998) in the two-dimensional case. Dgani & Soker (1994) considered radiative shocks with a mass loss term.

Recently, Yamada & Nishi (2001) investigated the stability properties of shock-compressed gas slabs by introducing a cold layer of finite thickness. They considered both symmetric and antisymmetric modes and reported the existence of quasi-oscillatory modes, in addition to the overstable ones.

Stability properties of radiative shocks with unequal ion and electron temperatures were investigated by Imamura et al. (1996), while flows with multiple cooling functions (i.e. bremsstrahlung and cyclotron) were examined both in the single and two-temperature regimes by Saxton et al. (1997), Saxton et al. (1998), Saxton (1999), Saxton & Wu (1999), Saxton & Wu (2001) and Saxton (2002). Additional references can be found in the review by Wu (2000).

Investigation of the full time-dependent problem has also received extensive attention over the past two decades and several numerical simulations have been carried along. The oscillatory instability was discovered in the first place numerically by Langer et al. (1981, LCSa hereafter) and Langer et al. (1982, LCSb hereafter), who investigated spherically symmetric accretion onto magnetized white dwarfs. They showed that flows with volumetric cooling rates  $\Lambda \sim \rho^2 T^\alpha$  become unstable when  $\alpha \lesssim 1.6$ , a limit subsequently revised to

$\alpha \lesssim 0.6$  in Langer et al. (1983). In the case of bremsstrahlung cooling ( $\alpha = 1/2$ ), the shock position was shown to undergo periodic oscillations over the surface of the white dwarf. Imamura et al. (1984, IWD hereafter) and Imamura (1985) used a Lagrangian code to investigate the stability of radiative shocks with a power-law cooling function  $\Lambda \sim \rho^2 T^\alpha$ . Effects of gravity, thermal conduction and unequal electron and ion temperatures were also included. In IWD, the critical values of  $\alpha$  (above which oscillations are damped) were shown to lie somewhere in the range  $1/3 \lesssim \alpha \lesssim 1/2$  and  $1/2 \lesssim \alpha \lesssim 0.6$  for the fundamental and first-overtone, respectively. Wolff et al. (1989) considered both one and two-temperature calculations; the one-temperature calculations showed that the fundamental mode is unstable for  $\alpha = 0.33$ , first and second harmonic are unstable when  $\alpha = 0.65$ , while the system is stable at  $\alpha = 1$ . The one-dimensional calculations of Strickland & Blondin (1995, SB hereafter) showed that for flows incident into a wall, large amplitude oscillations are damped when  $\alpha \gtrsim 0.5$ . SB also considered perturbed steady-state models, showing that power-law cooling functions with  $\alpha \lesssim 0.75$  produced shock oscillations which saturated at a finite amplitude. The results of SB were recently extended by Sutherland et al. (2003, SBD hereafter) to a more realistic cooling function.

Most results of the previous numerical investigations, however, bear no clear relation with the predicted linear behavior, and a direct comparison with perturbative studies has proven to be only partially successful. Although the salient features of thermally unstable shocks have been commonly reproduced, the modes of instabilities can not always be identified with the linear ones, with the exception of one or two modes. Besides, controversies exist on the value of the critical  $\alpha$  above which the system should become stable. These apparent inconsistencies may be partially due to the fact that most calculations do not include a stationary solution in their initial condition, which makes the problem inherently nonlinear since the very beginning. Moreover, a substantial disagreement exists between Eulerian and Lagrangian calculations and on the numerical treatment of the lower boundary condition which plays a crucial role in the dynamics of the post shock flow.

Here I wish to present some new and detailed calculations in the attempt to settle part of these controversies. The results of this work will also serve as a basis for future extensions, where effects of magnetic fields and more realistic cooling functions will be considered.

The paper is organized as follows. In §2 the problem is defined and the relevant equations are introduced. In §3 the stability properties of 1-D planar radiative shocks are reviewed in more detail, while in §4 numerical simulations are presented with particular emphasis to the comparison with linear theory and to the choice of boundary conditions. A new time-dependent treatment of the lower boundary is introduced and the details of implementation are given in Appendix A.

## 2. STATEMENT OF THE PROBLEM AND EQUATIONS

Consider a one-dimensional supersonic flow with uniform density  $\rho_{\text{in}}$  and velocity  $v_{\text{in}}$ , initially propagating in the negative x-direction, i.e.,  $v_{\text{in}} = -|v_{\text{in}}|$ . The flow is brought to rest by the presence of a rigid wall located at  $x = 0$ , and a shock wave forms at some finite distance  $x_s$  from the wall. Through the shock, the bulk kinetic energy of the incoming gas is converted into thermal motion and the flow decelerates to subsonic velocities. In the postshock region, the thermal energy of the accreting gas is radiated away by cooling processes.

In steady-state, the dynamical time scale is equal to the cooling time scale, so a fluid element travels through the postshock region and cools exactly to zero temperature by the time it reaches the wall.

In several areas of interest and to make the problem more tractable, radiative losses are treated in the optically thin regime and the cooling rates are normally specified as functions of the temperature, density and relative abundances. In this work it is assumed that the volumetric cooling rates can be described by a single power-law (in temperature) function

$$\Lambda(\rho, p) = a\rho^2 \left( \frac{p}{\rho} \right)^\alpha, \quad (1)$$

where  $a$  is a physical constant depending on the particular cooling process,  $\alpha$  is the cooling index and  $\rho$  and  $p$  are, respectively, the density and pressure of the gas.

The problem of a supersonic flow into a wall is, of course, a simplified abstraction of a more complex and specific physical setting. Effects due to thermal conduction, magnetic fields and multi-dimensional effects are neglected in this paper and will be considered in future works. With these assumptions, the problem can be described by the Euler equations for a one-temperature flow in planar geometry:

$$\frac{\partial \rho}{\partial t} + \rho \frac{\partial v}{\partial x} + v \frac{\partial \rho}{\partial x} = 0, \quad (2)$$

$$\frac{\partial v}{\partial t} + v \frac{\partial v}{\partial x} + \frac{1}{\rho} \frac{\partial p}{\partial x} = 0, \quad (3)$$

$$\frac{\partial p}{\partial t} + v \frac{\partial p}{\partial x} + \gamma p \frac{\partial v}{\partial x} = -(\gamma - 1) \mathcal{C} \rho^2 \left( \frac{p}{\rho} \right)^\alpha, \quad (4)$$

where  $v$  is the fluid velocity,  $\mathcal{C}$  is a constant and an ideal equation of state with constant specific heat ratio  $\gamma$  has been assumed. Equations (2) through (4) are put in a dimensionless form by expressing density and velocity in units of their inflow values, i.e.,  $\rho_{\text{in}}$  and  $|v_{\text{in}}|$ . With this choice, the flow variables immediately ahead of the shock become  $\rho = 1$ ,  $v = -1$  and  $p = 1/(\gamma \mathcal{M}^2)$ , with  $\mathcal{M}$  being the upstream Mach number.

The length scale of the problem enters explicitly through the constant  $\mathcal{C}$  in the energy equation (4):

$$\mathcal{C} = L_c a \rho_{\text{in}}^{1-2\alpha} |v_{\text{in}}|^{2\alpha-3}, \quad (5)$$

where  $L_c$  sets the reference length scale and  $a$  has already been introduced in equation (1). In the following, lengths will be conveniently normalized to the stationary thickness of the cooling region, so that the equilibrium position of the shock is  $x = 1$ . The explicit expression for  $\mathcal{C}$  is given in §3.1.

Relations between quantities ahead and behind the shock follow from the Rankine-Hugoniot jump conditions:

$$-v_s = \frac{1}{\rho_s} = \frac{\gamma - 1}{\gamma + 1} + \frac{2}{(\gamma + 1) \mathcal{M}^2}, \quad (6)$$

$$p_s = \frac{2}{\gamma + 1} - \frac{\gamma - 1}{\gamma(\gamma + 1) \mathcal{M}^2}, \quad (7)$$

where quantities immediately behind the shock are denoted with the subscript  $s$ , and  $\gamma = 5/3$  will be used in what follows.

### 3. LINEAR THEORY

Equilibrium configurations of radiative shock waves may be thermally unstable. The nature of the instability may be interpreted as follows.

Consider a stationary shock, initially in equilibrium; if, say, the postshock temperature is slightly increased, a longer cooling path will result and the excess pressure will force the shock to move upward. In the frame of the shock, the velocity of the incoming gas will increase even further and the postshock temperature will rise according to the square of the preshock velocity. If radiative losses are described by a decreasing function of the temperature, the cooling time will increase and the shock will continue to move upward.

### 3.1. Perturbative Analysis

A perturbative study is carried out by properly linearizing equations (2)–(4) around the steady-state solutions denoted with  $\rho_0$ ,  $v_0$  and  $p_0$ . The perturbed location of the shock front is written as

$$x_s = 1 + \frac{\epsilon}{\delta} e^{\delta t}, \quad (8)$$

where  $x_s = 1$  is the shock equilibrium position in absence of perturbation ( $\epsilon = 0$ ),  $\epsilon$  is the magnitude of the perturbation, and  $\delta$  is a complex eigenfrequency. According to the normalization scales introduced in §2, time is expressed in units of  $L_c/|v_{\text{in}}|$ .

Following the same notations as in Saxton et al. (1998), it is convenient to write  $\delta = \delta_R + i\delta_I$ , where the real part  $\delta_R$  gives the growth/decay term, while  $\delta_I$  represents the oscillation frequency. The nature of the instability is determined by the sign of  $\delta_R$ : modes with negative  $\delta_R$  are stable, while modes with positive  $\delta_R$  are unstable.

Perturbed physical variables take the form

$$q(\xi, t) = q_0(\xi) \left( 1 + \lambda_q(\xi) \epsilon e^{\delta t} \right), \quad (9)$$

where  $q \in \{\rho, v, p\}$ ,  $q_0(\xi)$  is the corresponding steady-state value and the complex function  $\lambda_q(\xi)$  describes the effects of the perturbation. Here  $\xi$  is a spatial coordinate normalized so that  $\xi = 1$  at the shock and  $\xi = 0$  at the wall:

$$\xi = \frac{x}{x_s} \approx x \left( 1 - \frac{\epsilon}{\delta} e^{\delta t} \right) + O(\epsilon^2). \quad (10)$$

The fluid equations are linearized in a frame of reference which is co-moving with the shock; in this frame the derivatives of a flow variable become

$$\frac{\partial}{\partial t} \rightarrow \frac{\partial}{\partial t} + \frac{\partial \xi}{\partial t} \frac{\partial}{\partial \xi}, \quad \frac{\partial}{\partial x} \rightarrow \frac{\partial \xi}{\partial x} \frac{\partial}{\partial \xi}. \quad (11)$$

Therefore, retaining only terms up to first order in  $\epsilon$ , one has

$$\frac{\partial q}{\partial t} \approx \left( q_0 \lambda_q \delta - \xi q'_0 \right) \epsilon e^{\delta t}, \quad (12)$$

$$\frac{\partial q}{\partial x} \approx q'_0 + \left( q'_0 \lambda_q + q_0 \lambda'_q - \frac{q'_0}{\delta} \right) \epsilon e^{\delta t}, \quad (13)$$

where a primed quantity denotes a derivative with respect to  $\xi$ .

The steady-state equations are obtained by collecting the zeroth order terms in the Euler equations; conservation of mass and momentum is trivially expressed by

$$\rho_0 v_0 = -1, \quad (14)$$

$$-v_0 + p_0 = m, \quad (15)$$

where the integration constants on the right hand sides may be evaluated from the preshock values; hence  $m = 1 + 1/(\gamma\mathcal{M}^2)$ .

The pressure equation provides the explicit dependence on the spatial coordinate; it can be put in closed integral form by writing

$$\xi(v_0) = \frac{f(v_0)}{f(v_s)}, \quad (16)$$

where

$$f(v) = \int_0^v (-y)^{2-\alpha} \frac{[y + \gamma(m+y)]}{(m+y)^\alpha} dy, \quad (17)$$

and  $v_s = -(1 + 3/\mathcal{M}^2)/4$  is the fluid velocity immediately behind the shock (eq. [6]). Notice that, according to the normalization units introduced in §2, the constant  $\mathcal{C}$  in equation (5) takes the value

$$\mathcal{C} = -\frac{f(v_s)}{(\gamma-1)}. \quad (18)$$

Results pertinent to this section are evaluated in the strong shock limit,  $\mathcal{M} \rightarrow \infty$ , so  $m = 1$ ,  $v_s = -1/4$  and  $\alpha$  becomes the only free parameter in the problem.

The integral in equation (17) can be evaluated analytically for some specific values of the cooling index  $\alpha$  (CI) but it has to be computed by numerical quadrature in the general case. Notice that a steady-state solution is possible only if the integral converges, that is, if  $\alpha < 3$ . Equation (16) can be inverted numerically to express the postshock steady flow velocity  $v_0$  as a function of  $\xi$ . The steady-state profiles are shown in Figure 1.

The first-order terms in  $\epsilon$  provide three coupled complex differential equations for the perturbations; using the unperturbed postshock velocity  $v_0$  as the independent variable, they are

$$\frac{d\lambda_p}{dv_0} + \frac{d\lambda_v}{dv_0} = -\frac{\xi}{v_0^2} - \frac{\lambda_p \delta}{v_0} \frac{d\xi}{dv_0}, \quad (19)$$

$$v_0 \frac{d\lambda_v}{dv_0} - p_0 \frac{d\lambda_p}{dv_0} = -\lambda_v \delta \frac{d\xi}{dv_0} + \frac{\xi}{v_0} + \lambda_p - 2\lambda_v - \lambda_p, \quad (20)$$

$$v_0 p_0 \left( \gamma \frac{d\lambda_v}{dv_0} + \frac{d\lambda_p}{dv_0} \right) = (v_0 + \gamma p_0) \left[ (2-\alpha)\lambda_p + (\alpha-1)\lambda_p - \lambda_v + \frac{1}{\delta} \right] - p_0 \lambda_p \delta \frac{d\xi}{dv_0} + \xi, \quad (21)$$

where  $d\xi/dv_0$  is given by straightforward differentiation of equation (16) together with equation (17).

For a given value of  $\alpha$ , equations (19) through (21) have to be solved by integrating from the shock front, where  $v_0 = v_s$ , to the wall, where  $v_0 = 0$ . The eigenmodes of the system are determined by imposing appropriate boundary conditions to select the physically relevant solutions. At the shock front the jump conditions for a strong shock ( $\mathcal{M} \rightarrow \infty$ ) apply (Imamura et al. 1996; Saxton et al. 1998):

$$\lambda_p = 0, \quad \lambda_v = -3, \quad \lambda_p = 2. \quad (22)$$

At the bottom of the postshock region ( $\xi = 0$ ) the relevant physical solutions must satisfy the stationary wall condition, namely, that the flow comes to rest and the velocity must be oscillation-free. This requires that both the real and imaginary parts of  $\lambda_v(v_0)$  vanish at  $v_0 = 0$ . The complex frequencies  $\delta$  for which such solutions are possible identify the eigenmodes of the system.

The method of solution adopted here consists in minimizing the real function of two variables  $\eta(\delta_R, \delta_I) = |\lambda_v(0)|$ . Here  $|\lambda_v(0)| = (\lambda_{v,R}^2(0) + \lambda_{v,I}^2(0))^{1/2}$  is the magnitude of the velocity perturbation at the bottom of the postshock region; the values of the real and imaginary parts,  $\lambda_{v,R}(0)$  and  $\lambda_{v,I}(0)$ , are obtained by direct numerical integration of equations (19)–(21) for a given pair  $(\delta_R, \delta_I)$ . In practice, since the system is singular at the origin, integration proceeds from the shock up to some small value of  $v_0$ , denoted with  $v_\epsilon$ . Setting  $v_\epsilon \lesssim 10^{-3}$  did not produce significant variations in the solution.

A preliminary coarse search with trial values of  $\delta_R$  and  $\delta_I$  shows that, for a given value of  $\alpha$ , an indefinitely long series of modes exists. Following CI, modes are labeled by increasing oscillation frequency, so that  $n = 0$  correspond to the fundamental mode,  $n = 1$  to the first overtone,  $n = 2$  to the second overtone, and so on. The approximate position of each mode  $n$ ,  $(\delta_R^{(n)}, \delta_I^{(n)})$ , is then iteratively improved by repeating the search on finer sub-grids (in the complex  $\delta$  plane) centered around the most recent iteration of  $\delta_R^{(n)}, \delta_I^{(n)}$ . The process stops once the relative error between two consecutive iterations falls below  $10^{-6}$ . For practical reasons, the search algorithm has been restricted to the first eight modes for values of  $\alpha$  uniformly distributed in the range  $-2 \leq \alpha < 2$ . Results are shown in Figures 2 and 3, while modes for some specific values of  $\alpha$  are listed in Tables 1 and 2.

A mode is stable if the real part of the corresponding eigenvalue has negative sign, and unstable otherwise. High-frequency modes are characterized by growth rates which decrease faster than low-frequency ones for increasing  $\alpha$ . Hence, the fundamental mode ( $n = 0$ ) has the smallest growth/damping rate for  $\alpha \lesssim 1$ , but the smallest damping rate for  $\alpha \gtrsim 1$ . Modes with  $n \geq 1$  have monotonically decreasing oscillation frequencies while, for the fundamental mode,  $\delta_I$  reaches a maximum value at  $\alpha \approx 1.1$  and decreases afterwards.

### 3.2. Critical $\alpha$

For each mode  $n$ , a critical value of the cooling index,  $\alpha_c^{(n)}$ , may be defined, such that  $\delta_R^{(n)} = 0$  when  $\alpha = \alpha_c^{(n)}$ . Hence, the  $n$ -th mode is stable for  $\alpha > \alpha_c^{(n)}$  and unstable when  $\alpha < \alpha_c^{(n)}$  (Fig. 4). The value of the critical  $\alpha$  is computed by interpolating  $\alpha$  with a quartic polynomial passing through the two pairs of values across which  $\delta_R$  changes sign. Thus the fundamental mode becomes stable for  $\alpha > 0.388$ , the first harmonic for  $\alpha > 0.782$ , and so on. Values of  $\alpha_c$  are listed in Table 2 and shown in Figure 4. Interestingly, the sequence of critical  $\alpha$  is not monotonic with increasing  $n$ . Finally, notice that all (8) modes become eventually stable for  $\alpha \gtrsim 0.92$ .

### 3.3. Linear Fit

By inspecting Figure 3, one can easily see that, for a given  $\alpha$ , the oscillation frequencies of the different modes are approximately equally spaced as  $n$  increases. In this respect, they resembles the modal frequencies of a pipe open at one end (Tóth & Draine 1993; Saxton et al. 1998; Saxton 1999) and can be described by a simple linear fit of the form

$$\delta_I^{(n)} = \tilde{\delta}_I^{(0)} + n\Delta\tilde{\delta}_I. \quad (23)$$

with a small residual,  $\lesssim 0.5\%$ . In equation (23),  $\tilde{\delta}_I^{(0)}$  is the “fitted” fundamental frequency and  $\Delta\tilde{\delta}_I$  is a frequency spacing depending on the cooling index  $\alpha$ .  $\Delta\tilde{\delta}_I$  is monotonically decreasing for increasing  $\alpha$ . Values of  $\tilde{\delta}_I^{(0)}$  and  $\Delta\tilde{\delta}_I$  are given in Tables 1 and 2.

## 4. TIME-DEPENDENT NUMERICAL SIMULATIONS

The results of the previous sections indicate that radiative shocks in real astrophysical settings may be linearly unstable and thus far from an equilibrium configuration. This calls for the investigation of the full time-dependent problem where nonlinear effects may play a major role in the shock dynamics.

In what follows, the radiative shock evolution is analyzed through a set of numerical simulations for different values of the cooling index  $\alpha$ . The early evolutionary phases are of particular interest since they can be directly compared to the expected linear behavior, thereby providing an effective tool in validating the correctness of the numerical method and choice of boundary conditions. Nonlinear effects, on the other hand, describe the long-term dynamics of the shock and play a crucial role in determining whether a linearly stable mode may actually be nonlinearly unstable (Saxton 1999).

### 4.1. Numerical Method

The numerical approach followed here relies on the high-resolution shock-capturing methods (HRSC henceforth, see LeVeque (1998) and references therein). HRSC methods rely on a finite-volume, conservative discretization of the Euler equations, thus being particularly suitable in describing shock dynamics and, in general, modeling flow discontinuities.

The starting point is the system of equations (2) through (4) written in conservative form:

$$\frac{\partial \mathbf{U}}{\partial t} = -\frac{\partial \mathbf{F}}{\partial x} + \mathbf{S}, \quad (24)$$

where  $\mathbf{U} = (\rho, \rho v, E)$  is a vector of conservative quantities, while

$$\mathbf{F} = \begin{pmatrix} \rho v \\ \rho v^2 + p \\ (E + p)v \end{pmatrix}, \quad \mathbf{S} = \begin{pmatrix} 0 \\ 0 \\ -\mathcal{C}\rho^{2-\alpha}p^\alpha \end{pmatrix}, \quad (25)$$

are the flux and source term vectors, respectively. The total energy density  $E$  is expressed as the sum of internal and kinetic terms:

$$E = \frac{p}{\gamma - 1} + \frac{\rho v^2}{2}. \quad (26)$$

The system of equations (24) is solved numerically using *PLUTO*, a high-resolution Godunov-type code for astrophysical fluid dynamics (Mignone et al. 2005, in preparation).

With *PLUTO*, equations (24) are solved by operator splitting, i.e., by treating the advection term  $\partial \mathbf{F} / \partial x$  and the source term  $\mathbf{S}$  in separate steps. This approach is second order accurate in time if the two operators have at least the same accuracy and the order into which they are applied is reversed every time step (Strang 1968).

During the advection step, a high-resolution, shock capturing Godunov-type formulation is adopted. Second-order accuracy in space is based on a conservative, monotonic interpolation of the characteristic fields (Colella 1990). Third-order temporal accuracy is achieved by a multi-step Runge-Kutta TVD algorithm



(Gottlieb & Shu 1998):

$$\begin{aligned}\mathbf{U}_j^1 &= \mathbf{U}_j^n + \Delta t^n \tilde{\mathbf{R}}_j(\mathbf{U}^n), \\ \mathbf{U}_j^2 &= \frac{1}{4} \left( 3\mathbf{U}_j^n + \mathbf{U}_j^1 + \Delta t^n \tilde{\mathbf{R}}_j(\mathbf{U}^1) \right), \\ \mathbf{U}_j^{n+1} &= \frac{1}{3} \left( \mathbf{U}_j^n + 2\mathbf{U}_j^2 + 2\Delta t^n \tilde{\mathbf{R}}_j(\mathbf{U}^2) \right).\end{aligned}\tag{27}$$

Here  $\tilde{\mathbf{R}}_j(\mathbf{U})$  is a conservative, discretized approximation to the flux term on the right hand side of equation (24):

$$\tilde{\mathbf{R}}_j(\mathbf{U}) = -\frac{\tilde{\mathbf{F}}_{j+\frac{1}{2}} - \tilde{\mathbf{F}}_{j-\frac{1}{2}}}{\Delta x_j},\tag{28}$$

where  $j$  labels the computational zone with mesh spacing  $\Delta x_j$ . The numerical fluxes  $\tilde{\mathbf{F}}_{j\pm\frac{1}{2}}$  are computed using the approximate Riemann solver of Roe (1981). It should be mentioned that, although different numerical schemes have also been employed, no significant differences were found in the results presented in §4.3. The particular choice of Riemann solver and interpolation algorithm is quite common and represents a good trade-off between accuracy and computational time.

Cooling is treated in a separate source step, where

$$\frac{dE}{dt} = -\mathcal{C}\rho^{2-\alpha}p^\alpha,\tag{29}$$

with  $\mathcal{C}$  given by equation (18), is solved. Notice that only the internal energy is affected during the source step, while density and velocity remain constant with the values provided by the most recent advection step. Thus, the kinetic contribution to the total energy can be discarded and equation (29) provides an ordinary differential equation in the pressure variable only. Integration for a time step  $\Delta t^n$  can be done analytically:

$$p^{n+1} = \begin{cases} [p^{1-\alpha} - \Delta t^n \mathcal{C}(\gamma-1)\rho^{2-\alpha}(1-\alpha)]^{\frac{1}{1-\alpha}} & \text{if } \alpha \neq 1, \\ p \exp(-\mathcal{C}(\gamma-1)\Delta t^n \rho^{2-\alpha}) & \text{if } \alpha = 1, \end{cases}\tag{30}$$

where  $p$  and  $\rho$  are the pressure and density at the beginning of the source step and the suffix  $j$  has been omitted for clarity of exposition.

Radiative losses are identically zero for  $T < T_c$ , where  $T = p/\rho$  is a dimensionless temperature and  $T_c$  is the cutoff temperature, equal to the temperature of the incoming gas, i.e.,  $T_c = 1/(\gamma\mathcal{M}^2)$ .

## 4.2. Initial and Boundary conditions

The computational domain is the region  $x_0 \leq x \leq x_1$ , where  $x_0$  and  $x_1$  define the locations of the lower and upper boundaries, respectively. As in the previous sections, lengths are expressed in units of the cooling thickness in steady-state; hence the shock is initially located at  $x = 1$ .

Upstream, for  $1 < x < x_1$ , density, velocity and pressure are uniform and equal to the preshock values, i.e.  $\rho = 1$ ,  $v = -1$  and  $p = 1/(\gamma\mathcal{M}^2)$ . At  $x = x_1$  a constant supersonic inflow defines the upstream boundary condition. Here  $x_1 = 5$  and  $\mathcal{M} = 40$  will be used for all simulations. Downstream, for  $x_0 \leq x \leq 1$ , flow quantities are initialized to the steady-state solution given by equations (14) through (16). The location of the lower boundary  $x_0$  depends on the particular boundary condition adopted.

The implementation of a suitable boundary condition at the lower boundary poses a serious nontrivial problem for a number of different reasons. Close to the wall, density and velocity experience rapidly varying sharp gradients, thus demanding increasingly high resolution in order to resolve flow patterns. This, in turns, has the inevitable consequence of restricting the time step size in an explicit code. Although a number of different strategies have been proposed, there is no general agreement about what would be a “consistent” boundary condition. A comparison between four different approaches is considered in this paper and results are discussed in detail in the next sections.

A first approach consists in using a reflecting boundary condition (RFbc), commonly adopted (Plewa 1995, SB) to simulate the presence of a rigid wall or to enforce axial or planar symmetry. It imposes symmetric profiles (with respect to the “wall” position  $x_0 = 0$ ) on density and pressure, while the velocity is antisymmetric, i.e.,  $v(-x) = -v(x)$ . Hence at the lower boundary, the velocity is zero at all times while density and pressure have zero gradient.

A second approach adopts a “fixed”, time-independent boundary conditions (FXbc) where flow variables are kept constant at the steady-state values at  $x = x_0$ . In this case,  $x_0 = 10^{-3}$  can be safely used, since is put sufficiently close to the wall but such that the temperature at that point is still above the cutoff temperature. The cutoff temperature, therefore, has only the effect of preventing cooling in the upstream region.

I also introduce a new, third approach based on the characteristic boundary method (Thompson 1987, 1990), the details of which are given in Appendix A. Following the same approach used in §3.1, the velocity will be held constant at the steady-state value, whereas pressure and density are allowed to evolve with time. The “constant-velocity” boundary condition is hereafter referred to as CVbc.

Finally, a fourth recipe (SB, SDB, LCSb) is to further extend the domain in the downstream direction by placing a cold dense layer for  $x_{\text{low}} < x < x_0$ . Here  $x_{\text{low}} = -2$  is the new location of the lower boundary, while  $x_0 = 10^{-4}$  still lies inside the postshock region. Flow quantities have constant profiles, continuous at  $x = x_0$  and the temperature of the cold layer becomes approximately 2% of the temperature immediately behind the shock. For this boundary condition, the cutoff temperature was set equal to the temperature of the cold dense layer. At the back of the layer,  $x = x_{\text{low}}$ , an outflow boundary condition (OBbc) holds on density, velocity and pressure.

The onset of instability is triggered by the discretization error of the numerical scheme and no external, “ad hoc” perturbation is introduced, unless otherwise stated.

A uniform grid is used in the region  $x_0 \leq x \leq 1.4$ , whereas a second, geometrically stretched grid covers the rest of the upstream region,  $1.4 < x \leq 5$ . The extent of the uniform region has been chosen to ensure that the largest-amplitude oscillations would adequately be resolved.

Issues concerning grid resolution effects must not be underestimated. In fact, as outlined by Sutherland et al. (2003, SBD hereafter), sharp density gradients can be described with relatively limited accuracy because of numerical diffusion effects that cause high-density regions to “leak” mass into neighboring low-density zones. Since the cooling process is proportional to the square of density, radiative losses will generally be overestimated, causing abnormal, excessive cooling. Although this issue is intrinsic to any grid of finite size and cannot be completely removed, higher resolutions can considerably mitigate the problem. Furthermore, small-amplitude oscillations of the shock front can be adequately captured on finer grids.

For this reason, a grid of 2240 computational zones covers the extent of the uniform region for all numerical simulations presented in this paper. With this resolution, the postshock flow is initially resolved on 1600 points. The number of points for the stretched grid has virtually no influence on the solution and

is held fixed at 200 in all cases.

### 4.3. Results

The one-dimensional numerical simulations are carried out for five different values of  $\alpha$ , selected according to the linear analysis results presented in §3.

I first consider the case where  $\alpha = 0$ , since all modes have positive (linear) growth rates. Next,  $\alpha = 0.5$  and  $\alpha = 0.7$  are examined, since all the overtones save the fundamental have positive linear growth rates and are, therefore, unstable. The value  $\alpha = 0.8$  lies just above the instability limit of the first and second harmonics; therefore, as one can see from Table 2, only overtones with  $n \geq 3$  are expected to be unstable. Finally, I consider the case  $\alpha = 1$ , for which all the first eight modes have been shown to have negative growth rates and thus are stable.

#### 4.3.1. $\alpha = 0.0$

The time-evolution diagrams for the four boundary conditions presented in §4.2 are shown in the four panels of Figure 5 and the corresponding power spectra of the shock oscillations are shown in Figure 6.

Significant departure from the steady-state solution occurs most rapidly when the RFbc is employed. In this case, the amplitude of the oscillations rapidly increases with time and the system enters a nonlinear saturated regime around  $t \sim 20$  after a short-lived linear phase. The use of the RFbc yields oscillation frequencies which are found to be shifted with respect to the values obtained from linear analysis. This particular choice of boundary condition, in fact, forces the velocity to have a node at the location of the lower boundary, while density and pressure have an extremum. Since this condition is far from the equilibrium configuration (eqns. [14]–[16]), strong nonlinear perturbations originate in the postshock flow and steepen into secondary shocks at a high rate. This also contributes to the higher amplitude oscillations observed in this case. Not surprisingly, the power spectrum of the shock position, Figure 6, exhibits frequencies that are offset from the ones predicted by linear analysis. Notice that, since the mass flux through the lower boundary is zero and cooling is not effective for  $T < T_c$ , a cold layer of gas at  $T = T_c$  accumulates at the bottom of the cooling region (Fig. 5). Inside this layer, density is approximately constant and equal to  $\gamma\mathcal{M}^2$ , whereas waves propagate at the local sound speed,  $c_s \sim 1/\mathcal{M}$ .

In contrast, the CVbc and FXbc yield similar results and the system preserves profiles close to the initial steady-state values. The early phase of evolution ( $t \lesssim 60 \div 70$ ) is characterized by a linear growth of the perturbation, while, for  $t \gtrsim 80$ , the amplitude of the oscillations begins to saturate and the instability becomes nonlinear. During this phase the largest oscillation amplitudes reach  $\sim 25\%$  of the initial equilibrium position. The OBbc shows reduced amplitudes with respect to the previous cases. In addition, the linear phase is longer than the CVbc or FXbc, and the transition to the nonlinear regime occurs only for  $t \gtrsim 110$ .

The power spectra for the early phase of the evolution ( $0 < t < 41$ ) are plotted in Figure 6. Both the CVbc and FXbc yield eigenfrequencies that can be definitely identified with the theoretical values, with a bigger uncertainty in the fundamental mode, see Table 3. Results obtained with the OBbc are similar and the fundamental mode differs from the analytical expectation by less than 4%.

One should bear in mind, however, that the linear growth rate of the fundamental mode is a factor of

$\approx 6$  smaller than those of higher harmonics ( $1 \leq n \leq 7$ , see Table 2), and therefore modes with  $n \geq 1$  tend to saturate faster. For this reason, a representative sample of the linear phase must have a limited length in the time domain and, consequently, the power spectrum inevitably suffers from poor resolution at lower frequencies.

The situation is different when a longer portion ( $92 \lesssim t \lesssim 201$ ) of the shock position during the saturated regime is analyzed, see Figure 7. In this case, the predominant mode of instability is the first overtone, whereas the fundamental mode and the second harmonic contribute by less than 10% to the oscillatory cycle. Notice also that when the CVbc and FXbc are used, the prevalent frequency of oscillation differs from the linear prediction by  $\sim 10\%$ , but it coincides with the first harmonic when the OBbc is adopted.

In all cases, a main sequence of harmonics with increasing frequencies  $\Omega^{(I)}$ ,  $\Omega^{(II)}$ ,  $\Omega^{(III)}$ , etc., may be identified by inspecting Figure 7. These overtones have monotonically decreasing power and do not necessarily coincide with the linear modes, but result from nonlinear interactions. Nonlinearity enters through mode-mode coupling, as it is suggested by considering the frequency spacing between them (Table 4). For the CVbc and OBbc, in fact, the spacing appears to be either a multiple of the fundamental mode or equal to the first overtone. In the OBbc case, for instance, one has that  $\Omega^{(II)} - \Omega^{(I)} \approx \Omega^{(III)} - \Omega^{(II)} \approx \Omega^{(IV)} - \Omega^{(III)} \approx \Omega^{(I)}$ , i.e., the mode spacing is a multiple of the first overtone. A similar result holds in the CVbc case where, from Table 4, it can be verified that  $\Omega^{(II)} - \Omega^{(I)} \approx 3\Omega^{(0)}$ ,  $\Omega^{(III)} - \Omega^{(II)} \approx \Omega^{(IV)} - \Omega^{(III)} \approx \Omega^{(I)}$ , and so on.

Intermediate, secondary peaks associated with small-power modes appears between the main sequence overtones. Some of these modes have been identified and labeled in Figure 7 with  $\Omega^{(Ia)}$ ,  $\Omega^{(Ib)}$ ,  $\Omega^{(IIa)}$ ,  $\Omega^{(IIb)}$ , etc.. These secondary overtones may result from mode-mode coupling between the main sequence modes and the fundamental. This coupling is most evident for the CVbc, where one finds that  $\Omega^{(0a)} - \Omega^{(0)} \approx \Omega^{(Ia)} - \Omega^{(I)} \approx \Omega^{(II)} - \Omega^{(Ib)} \approx \Omega^{(0)}$ , and similarly for higher harmonics (see Tab. 4).

#### 4.3.2. $\alpha = 0.5, 0.7$

Based on the previous results and considerations, the CVbc, FXbc and OBbc yield results that more accurately reproduce the predicted linear behavior during the system’s early phase of evolution. Moreover, results obtained with the FXbc and CVbc exhibits strong similarities, and thus only the CVbc and OBbc will be considered in what follows.

The  $\alpha = 0.5$  value is of particular astrophysical relevance, since it describes optically thin bremsstrahlung, which is the main source of radiative losses at temperatures of the order of  $10^8 \div 10^9$  K, typical in accretion shocks in magnetic cataclysmic variables.

When the CVbc is adopted the system exhibits a linear phase for  $t \lesssim 150$ , gradually followed by the transition to the nonlinear regime. When compared to the  $\alpha = 0$  case, the oscillation amplitudes in the saturated regime are reduced by a factor of approximately 50%. The situation is quite different, however, when the OBbc is considered: Figure (8) shows that the solution remains close to the initial steady-state values and unstable oscillations grow at a smaller rate.

A similar behavior has been reported by SB95 (who also adopted an “open boundary” condition) for small values of the inflow Mach number (i.e.,  $\mathcal{M} = 5$ ). In their simulations, however, the amplitude of the oscillations was found to increase for higher Mach numbers, a behavior not observed in the present work. The present conclusion is supported by several supplementary tests in which both the inflow Mach number and the density of the cold layer were changed, but a fully nonlinear growth of the instability was

still never observed. In all the numerical tests, in fact, the cold gas layer always acts as an absorber to incoming perturbations, consequently reducing the amplitude of the reflected waves. Even in the presence of an external “ad hoc” perturbation (similar to the one introduced in SB95) it was found that the use of a cold dense “layer” inhibits the growth of instability when  $\alpha \gtrsim 0.45$ .

The behavior of the system during the early phases is reflected in the power spectra shown in Figure 9, where a positive identification of the oscillation eigenfrequencies with the linear ones is clear. The relative errors of the identifiable peaks are less than 4% for all modes, see Table 3. Notice that the fundamental mode (expected to be stable from the linear analysis) is also visible in the spectrum, since the initial numerical perturbation excites all modes regardless of their stability.

The power spectra taken during the later phases, Figure 10, reveal that, for the OBbc, the (mildly) unstable behavior is mostly sustained by the first three overtones, whereas the first harmonic is the only dominant mode for the CVbc. In both cases, little contribution is given by the fundamental mode. Nonlinear effects, however, suggest that the fundamental mode may still be important through mode-mode coupling. Similarly to the  $\alpha = 0$  case, in fact, a main sequence of modes can again be identified, see Figure 10. For the CVbc, the frequency spacing between these modes is either a multiple of the fundamental or equal to the first overtone, e.g.,  $\Omega^{(II)} - \Omega^{(I)} \approx 3\Omega^{(0)}$  and  $\Omega^{(IV)} - \Omega^{(III)} \approx \Omega^{(I)}$ . Secondary, small-power overtones are mainly visible for the OBbc case. Again, strong evidence for inter-mode coupling is supported by the fact that these secondary overtones may be decomposed into main sequence modes. In fact, if one consider the frequencies listed in Table 4, it can be seen that  $\Omega^{(0a)} \approx \Omega^{(I)} - \Omega^{(0)}$ ,  $\Omega^{(II)} - \Omega^{(Ia)} \approx \Omega^{(0)}$ ,  $\Omega^{(IIIa)} - \Omega^{(III)} \approx \Omega^{(0)}$ , and so on.

For  $\alpha = 0.7$ , an additional external perturbation has been introduced to catalyze the onset of instability. The perturbation is initially given in the velocity profile as

$$v_0(x) \implies v_0(x) \left( 1 + \epsilon \exp \left[ - \left( \frac{x - 0.5}{0.1} \right)^2 \right] \right), \quad (31)$$

with  $\epsilon = 0.05$ . Density and pressure are obtained according to equations (14) and (15).

The different behaviors of the OBbc and CVbc are illustrated in Figure 8. Results obtained with the OBbc show that the initial perturbation is damped roughly on a timescale  $t \sim 150$ . As for the  $\alpha = 0.5$  case, the cold dense layer behind the postshock region tends to quench large-amplitude perturbations. On the other hand, when the CVbc is adopted, the initial perturbation does not fade away and the instability grows at a small rate. The amplitude of the oscillations relative to initial shock position is now further reduced to  $\lesssim 5\%$  of the initial shock position. Table 3 shows that the eigenfrequencies of the oscillations differ by less than 8% from the theoretical results.

The power spectra for the early linear phase, Figure 9, are similar to the previous cases, although only modes with  $0 \leq n \leq 4$  (for the CVbc) and  $1 \leq n \leq 5$  (for the OBbc) contribute to the oscillations.

During the nonlinear phase (CVbc only), the first harmonic gives the largest contribution, while the third overtone account for roughly 10%, Figure 10. Although little power is present in the fundamental mode, the frequency spacing between main sequence harmonics seems to indicate that mode-mode coupling may account, one more time, for the secondary, small-power intermediate peaks ( $\Omega^{(Ia)}$ ,  $\Omega^{(Ib)}$ , etc.) shown in Figure 10. Some the  $\Omega$ 's are, in fact, closely related:  $\Omega^{(Ia)} \approx \Omega^{(II)} - \Omega^{(I)}$ ,  $\Omega^{(Ic)} \approx \Omega^{(III)} - \Omega^{(Ia)}$ ,  $\Omega^{(IIIa)} - \Omega^{(III)} \approx \Omega^{(0)}$ ,  $\Omega^{(IV)} - \Omega^{(III)} \approx \Omega^{(I)}$ , and so on.

### 4.3.3. $\alpha = 0.8, 1$

The simulations for the last two cases,  $\alpha = 0.8$  and  $\alpha = 1$ , are carried out using the CVbc only, since no growth of instability was observed using the OBbc. In both cases, the perturbation given by equation (31) was imposed at  $t = 0$ . Results are shown in Figures 11 and 12.

When  $\alpha = 0.8$ , the early phases of the evolution reflect the expected linear growth, as one can see from Figure 12. The power spectrum for to this phase shows modes of oscillations that clearly match the theoretical ones. Most of the power is contributed by the first harmonic, followed by the fundamental and then the remaining overtones.

The complete transition to the nonlinear phase occurs for  $t \gtrsim 200$ , where smaller-amplitude, higher-frequency oscillations take over. A power spectrum of the late evolution reveals the effects of this transition, Figure 12. Most of the power is concentrated in the third harmonic, with only  $\sim 10\%$  going into the first overtone and less than  $\sim 1\%$  into the second harmonic. The fundamental mode is absent.

The fact that high-frequency oscillations are dominated by the third harmonic is quite a remarkable result, since this overtone is the lowest unstable mode only in the narrow range  $0.795 < \alpha < 0.85$ , while modes with  $n < 3$  are stable as can be seen from Table 2. This strongly suggests that this particular choice of boundary condition is particularly consistent with linear results.

Notice that both the first and second harmonic should be linearly stable, since  $\alpha_c^{(1)} = 0.7815 < 0.8$  and  $\alpha_c^{(2)} = 0.795 < 0.8$ . Their presence in the power spectrum, however, indicate that a weak nonlinearity may probably be present. Besides, nonlinear interactions are likely to be responsible for the frequency coupling between the third and fourth main sequence overtones, since  $\Omega^{(IV)} \approx 2\Omega^{(III)}$ .

Finally, when  $\alpha = 1$ , the initial perturbation is damped and the system returns to the original equilibrium solution for  $t \gtrsim 70$ . The power spectrum of the early evolutionary phase (Fig. 12) shows that the shock oscillations are decomposed into frequency modes that are well approximated by linear results.

## 5. DISCUSSION

A study of planar radiative shocks with a power-law cooling function  $\Lambda \sim \rho^2 T^\alpha$  has been conducted. Both linear and nonlinear time-dependent calculations have been presented.

A linear stability analysis has been carried out for several values of the cooling index  $\alpha$  in the range  $[-2, 2)$ . For a given value of  $\alpha$ , multiple discrete modes of oscillation exist and the real and imaginary parts of the first eight eigenfrequencies have been derived. The overstable modes are labeled in order of increasing oscillation frequency so that  $n = 0$  corresponds to the fundamental mode,  $n = 1$  to the first overtone,  $n = 2$  to the second overtone, and so forth. The stability criterion of a particular mode is expressed by the condition  $\alpha > \alpha_c^{(n)}$ , where  $\alpha_c^{(n)}$  is the critical value of the cooling index for the  $n$ -th mode. For the fundamental mode, for example,  $\alpha_c^{(0)} = 0.388$ , whereas for the first and second harmonic  $\alpha_c^{(1)} = 0.782$  and  $\alpha_c^{(2)} = 0.795$ , respectively. A general trend towards stability exists for increasing  $\alpha$ , so eventually all modes are stabilized for  $\alpha \gtrsim 0.92$ . This study confirms previous results (CI), for which only the first two or three modes have been reported for some values of the cooling index. It has been shown that oscillation frequencies are linearly proportional to the mode number  $n$ , a behavior similar to the quantized modes in a pipe.

The perturbative study has been complemented by several numerical simulations using an Eulerian, high-resolution shock-capturing scheme. The shock evolution has been followed through the linear and nonlinear

phases for different values of  $\alpha$  and boundary conditions. Among the four boundary conditions under consideration (§4.2), a new time-dependent boundary treatment has been introduced. The new approach is based on the characteristic boundary method for the Euler equations and is particularly consistent with the basic assumptions used in the analytical work, where the velocity perturbation has a node at the wall.

For the most unstable case considered here ( $\alpha = 0$ ), all boundary conditions yield similar results, although the reflective wall boundary condition is not particularly suitable in modeling small departures from the stationary solution. The remaining three strategies provide modes of oscillations that, in the limit of small perturbations, are close (within 5% accuracy with the exception of the fundamental mode) to the analytical values.

The cases  $\alpha = 0.5, 0.7, 0.8$  and 1 have also been considered. For  $\alpha = 0.5, 0.7$ , the numerical simulations show that the choice of the lower boundary condition has a more severe impact on the growth of unstable modes during the saturated phase. For example, the additional cold dense layer used in the open boundary condition (§4.2) tends to inhibit large-amplitude oscillations and, for  $\alpha \gtrsim 0.7$ , totally prevents the growth of instability. In contrast, the new boundary approach yields results that closely reflect the analytical predictions; unstable behavior was observed for  $\alpha = 0.5, 0.7$ , and 0.8, although the saturated amplitude of oscillations considerably decreases with increasing  $\alpha$ . For  $\alpha = 0.8$ , the largest oscillations during the saturated phase are reduced to  $\sim 0.5\%$  of the initial shock position and are thus barely visible at the resolution adopted (1600 zones for the postshock flow). For  $\alpha = 1$ , the shock is stable and initial perturbations are damped on a characteristic timescale roughly proportional to the e-folding time of the first overtone. The modes of oscillations found in the numerical simulations (during the early phase of evolution) can be positively identified with the ones derived by linear analysis. The relative error is usually small,  $\lesssim 8\%$ . Notice that this error also accounts for the discrete frequency spacing introduced by the fast-Fourier transform of the shock position.

The transition from the linear to the nonlinear regime has also been investigated. Power spectra of the shock position during the late evolutionary phases reveal that the first overtone is the dominant mode of oscillation when  $\alpha \lesssim 0.7$ , but that the third harmonic contributes to most of the power at  $\alpha = 0.8$ . The contribution of the fundamental is only 10% for the most unstable case ( $\alpha = 0$ ), and decreases for increasing  $\alpha$ .

The new result of this work shows that a main sequence of overtones characterizes the saturated, nonlinear oscillatory phases. Additional, secondary modes may also be present, depending on the particular choice of boundary condition. These modes of oscillation do not always match those predicted by linear analysis but result from complex nonlinear interactions. For the first time, evidence has been provided in favour of mode-mode coupling, particularly between the first harmonic and the fundamental mode. The result extends also to those cases in which some of the modes are linearly stable ( $\alpha = 0.5, 0.7, 0.8$ ), thus supporting the possibility that linearly stable modes may actually become nonlinearly unstable.

In summary, a general trend towards stability is found for  $\alpha \gtrsim 0.8$ , while an unstable behavior is expected for  $\alpha \lesssim 0.4$ , regardless of the choice of the lower boundary condition. On the other hand, numerical models of radiative shocks are more sensitive to the treatment of the lower boundary condition when  $0.4 \lesssim \alpha \lesssim 0.8$ , a range particularly relevant when optically thin bremsstrahlung is the dominant cooling mechanism. It should be pointed out that the use of a cold layer of finite thickness may be more self-consistent in realistic astrophysical applications. The existence of the layer is, in fact, automatically induced by a cutoff temperature in the cooling function and avoids the complication of specifying a boundary conditions at the interface between the postshock flow and the layer (provided the sharp density gradients present in this

region are adequately captured).

In spite of the oversimplifying assumptions adopted in this study, these results show a number of interesting consequences for a variety of astrophysical settings.

Radiative shocks with velocities  $v_s \gtrsim 130 \text{ km s}^{-1}$  are not uncommon in jets from young stellar objects, supernova remnants in the radiative phase, magnetospheric accretion in T-Tauri stars, and colliding stellar winds in relatively close binary systems. For these systems, the shocked interstellar gas reaches temperatures in the range  $10^5 - 10^7 \text{ K}$  and cools mainly by line emission, for which  $\alpha < -0.5$ . Under these conditions, radiative shocks are likely to show unstable behavior in all modes and phenomenological interpretations based on steady-state models become of questionable validity (Innes et al. 1987a,b). Although inclusion of transverse magnetic fields extends the range of stability (Smith 1989; Tóth & Draine 1993), the global thermal instability of radiative shock waves may still be important in interpreting a number of distinct observational features, such as emission-line ratios observed in interstellar radiative shocks (Hartigan et al. 1994), mixing between hot and cold material in colliding winds (Stevens et al. 1992; Antokhin et al. 2004), the filamentary structures observed in supernova remnants (Blondin et al. 1998; Walder & Folini 1998), and so forth.

Less conclusive assertions can be made for standing shocks in the accretion columns of Polar and Intermediate Polar systems. At temperatures of the order of  $10^8 - 10^9 \text{ K}$  the X-ray emission is primarily determined by optically thin bremsstrahlung, although cyclotron and Compton cooling may not be neglected (Saxton et al. 1998). However, in the simple case where radiative losses are due to bremsstrahlung cooling only,  $\alpha \approx 0.5$ , the dynamics of the shock may be influenced by the interaction with the upper photospheric layers of the white dwarf (Cropper 1990). Hence realistic models of accretion columns may require a more complex treatment of the lower boundary. For this reason, inclusion of additional physical processes such as magnetic fields, multi-dimensional effects, thermal conduction, etc., might be crucial for drawing firm conclusions about the stability of radiative shocks in AM-Her-type systems. Some of these issues will be considered in future extensions of this work.

The author would like to thank T. Plewa, B. Rosner, A. Königl, D. Q. Lamb, and T.J. Linde for their constructive support during my Ph.D. research program at the University of Chicago.

## A. CHARACTERISTIC BOUNDARY CONDITIONS

The hyperbolic nature of the Euler equations requires boundary conditions to be specified according to the way information propagates in and out of the boundary. The novel approach introduced in §4.2 is based on the characteristic boundary method (Thompson 1987, 1990), where “physical” and “numerical” boundary conditions specify how zone boundary values are integrated in time along with the interior values. Although the subject of boundary conditions is a vast one and falls outside the scope of this paper, details of implementation are given hereafter.

A “physical” boundary condition describes information that enters the domain and thus has to be imposed for each characteristic wave that propagates from the boundary towards the inside. Information directed outside the boundary is entirely determined by the solution inside the domain and thus does not require a boundary condition. The numerical scheme, however, still depends on the knowledge of all flow variables at boundary zones, and hence additional “numerical” boundary conditions must be prescribed in a consistent way.



In the present context, the boundary equations are more conveniently formulated using the quasi-linear form

$$\frac{\partial}{\partial t} \begin{pmatrix} \tau \\ v \\ p \end{pmatrix} + \begin{pmatrix} v & -\tau & 0 \\ 0 & v & \tau \\ 0 & \gamma p & v \end{pmatrix} \frac{\partial}{\partial x} \begin{pmatrix} \tau \\ v \\ p \end{pmatrix} = \begin{pmatrix} 0 \\ 0 \\ -(\gamma - 1)\Lambda \end{pmatrix} \quad (\text{A1})$$

where  $\tau = 1/\rho$ . The system of equations (A1) holds at the boundary and must evolve in time together with the interior values. The characteristic speeds of the system (A1) are given by  $\lambda^\pm = v \pm c_s$ ,  $\lambda^0 = v$ , where  $c_s = (\gamma p/\rho)^{1/2}$  is the speed of sound.

In the postshock region the flow is initially subsonic everywhere, since  $-c_s < v < 0$  for  $0 < x < 1$ . In the limit of small perturbations around the steady-state values, it is reasonable to assume that a condition for subsonic outflow will continue to hold at subsequent times. Hence, the characteristic associated with  $\lambda^+$  has positive sign (i.e., it carries information inside the domain), whereas  $\lambda^0$  and  $\lambda^-$  are directed outward. This means that only one “physical” boundary condition can be freely specified (e.g., a constant pressure or velocity) and the remaining two must be compatible with the interior discretization scheme. Choosing a constant outflow velocity, for example, is consistent with the linear perturbative analysis, where the velocity perturbation is forced to have a node at the origin.

Integration of the boundary equations (A1) proceeds by splitting the time-dependent solution into a contribution coming from the steady-state value and a time-dependent “deviation”:

$$q(x, t) = q_1(x, t) + q_0(x) \quad (\text{A2})$$

where  $q \in \{\tau, u, p\}$ . In the “constant-velocity” boundary condition, the velocity perturbation  $v_1 = 0$  at all times and the boundary equations prescribe how pressure and density should evolve with time:

$$\frac{\partial \tau_1}{\partial t} + v_0 \frac{\partial \tau_1}{\partial x} - \tau \frac{\partial v_1}{\partial x} = \tau_1 \frac{\partial v_0}{\partial x}, \quad (\text{A3})$$

$$\frac{\partial p_1}{\partial t} + v_0 \frac{\partial p_1}{\partial x} + \gamma p \frac{\partial v_1}{\partial x} = -(\gamma - 1)(\Lambda - \Lambda_0) - \gamma p_1 \frac{\partial v_0}{\partial x}, \quad (\text{A4})$$

where the spatial derivatives are computed using one-sided approximations. Notice that equations (A3) and (A4) are not a linearization around a stationary solution but are, in principle, valid for arbitrary departures.

## REFERENCES

- Antokhin, I. I., Owocki, S. P., & Brown, J. C. 2004, ApJ, 611, 434
- Bertschinger, E. 1986, ApJ, 304, 154
- Blondin, J. M., Wright, E. B., Borkowski, K. J., & Reynolds, S. P. 1998, ApJ, 500, 342
- Calvet, N. & Gullbring, E. 1998, ApJ, 509, 802
- Chanmugam, G., Langer, S. H., & Shaviv G. 1985, ApJ, 299, L87
- Chevalier, R. A. & Imamura, J. M. 2003, ApJ, 261, 543
- Colella, P. 1990, ApJ, 54, 174.

- Cropper, M. 1990, *Space Sci. Rev.*, 54, 195
- Dgani, R., & Soker, N. 1994, *ApJ*, 434, 262
- Edelman, M. A. 1989, *Astrofizika*, 31, 407 (English transl., *Astrophysics*, 31 656 [1990])
- Edelman, M. A. 1989, *Astrofizika*, 31, 579 (English transl., *Astrophysics*, 31 758 [1990])
- Gaetz, T. J., Edgar, R. J., & Chevalier, R. A. 1988, *ApJ*, 329, 927
- Gottlieb, S. & Shu, C. W. 1998, *Math. Comput.*, 67, 73
- Hartigan, P., Morse, J. A., & Raymond, J. 1994, *ApJ*, 436, 125
- Houck, J. C. & Chevalier, R. A. 1992, *ApJ*, 395, 592
- Hujeirat, A., & Papaloizou, J. C. B. 1998, *A&A*, 340, 593
- Imamura, J. N., Wolff, M. T., & Durisen, R. H. 1984, *ApJ*, 276, 667
- Imamura, J. N. 1985, *ApJ*, 296, 128
- Imamura, J. N., Rashed, H., & Wolff, M. T. 1991, *ApJ*, 378, 665
- Imamura, J. N., Aboasha, A., Wolff, M. T. & Wood, S. W. 1996, *ApJ*, 458, 327
- Innes, D. E., Gidding, J. R., & Falle, S. A. E. G. 1987, *MNRAS*, 226, 67
- Innes, D. E., Gidding, J. R., & Falle, S. A. E. G. 1987, *MNRAS*, 227, 1021
- Kimoto, P. A., & Chernoff, D. F. 1997, *ApJ*, 485, 274
- Langer, S. H., Chanmugam, G., & Shaviv, G. 1981, *ApJ*, 245, L23
- Langer, S. H., Chanmugam, G., & Shaviv, G. 1982, *ApJ*, 258, 289
- Langer, S. H., Chanmugam, G., & Shaviv, G. 1982, in *Cataclysmic Variables and Related Objects*, ed. M. Livio and G. Shaviv (Dordrecht: Reidel), p. 199
- Larsson, S. 1992, *A&A*, 265, 133
- LeVeque, R. J., Mihalas, D., Dorfi, E. A., & Müller, E. 1998, *Computational Methods for Astrophysical Flow*: Springer-Verlag
- Middleditch, J., Imamura, J. N., & Steiman-Cameron, T. Y. 1997, *ApJ*, 489, 912
- Plewa, T. 1995, *MNRAS*, 275, 143
- Roe, P. L. 1981, *J. Comp. Phys.*, 43, 357
- Saxton, C. J., Wu, K., & Pongracic, H. 1997, *PASA*, 14, 164
- Saxton, C. J., Wu, K., Pongracic, H., & Shaviv, G. 1998, *MNRAS*, 299, 862
- Saxton, C. J. 1999, Ph.d. Thesis, University of Sydney.
- Saxton, C. J., & Wu, K. 1999, *MNRAS*, 310, 677

- Saxton, C. J., & Wu, K. 2001, MNRAS, 324, 659
- Saxton, C. J. 2002, PASA, 19, 282
- Smith, M. D. 1989, MNRAS, 238, 235
- Stevens, I. R., Blondin, J. M., & Pollock, A. M. T. 1992, ApJ, 386, 265
- Strang, G. 1968, SIAM J. Num. Anal., 5, 506
- Strickland, R. & Blondin, J. M. 1995, ApJ, 449, 727
- Sutherland, R. S., Bicknell, G. V., & Dopita, M. A. 2003, ApJ, 591, 238
- Thompson, K. W. 1987, JCP, 68, 1
- Thompson, K. W. 1990, JCP, 89, 439
- Tóth, G. & Draine, B. T. 1993, ApJ, 413, 176
- Walder, R. & Folini, D. 1998, A&A, 330, L21
- Wolff, M. T., Gardner, J. H., & Wood, K. S. 1989, ApJ, 346, 833
- Wood, K. S., Imamura, J. N., & Wolff, M. T. 1992, ApJ, 398, 593
- Wu, K., Chanmugam, G., & Shaviv, G. 1992, ApJ, 397, 232
- Wu, K., Pongracic, H., Chanmugam, G., & Shaviv, G. 1996, PASA, 13, 93
- Wu, K. 2000, Space Sci. Rev., 93, 611
- Yamada, M. & Nishi, R. 2001, ApJ, 547, 99

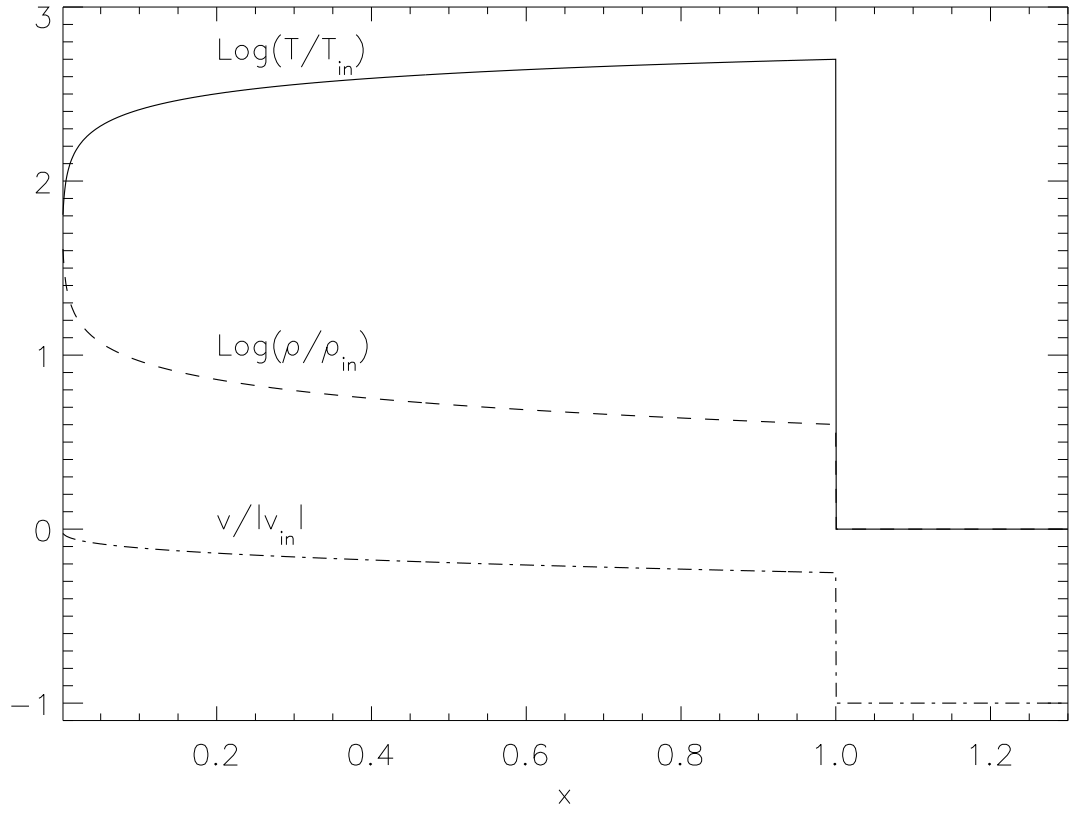


Fig. 1.— Steady-state profiles for density, temperature and velocity when  $\alpha = 0$ . The “wall” is located at  $x = 0$  and supersonic gas flows from the right to the left. Flow variables are normalized to their inflow values, and the abscissa is expressed in units of shock height.

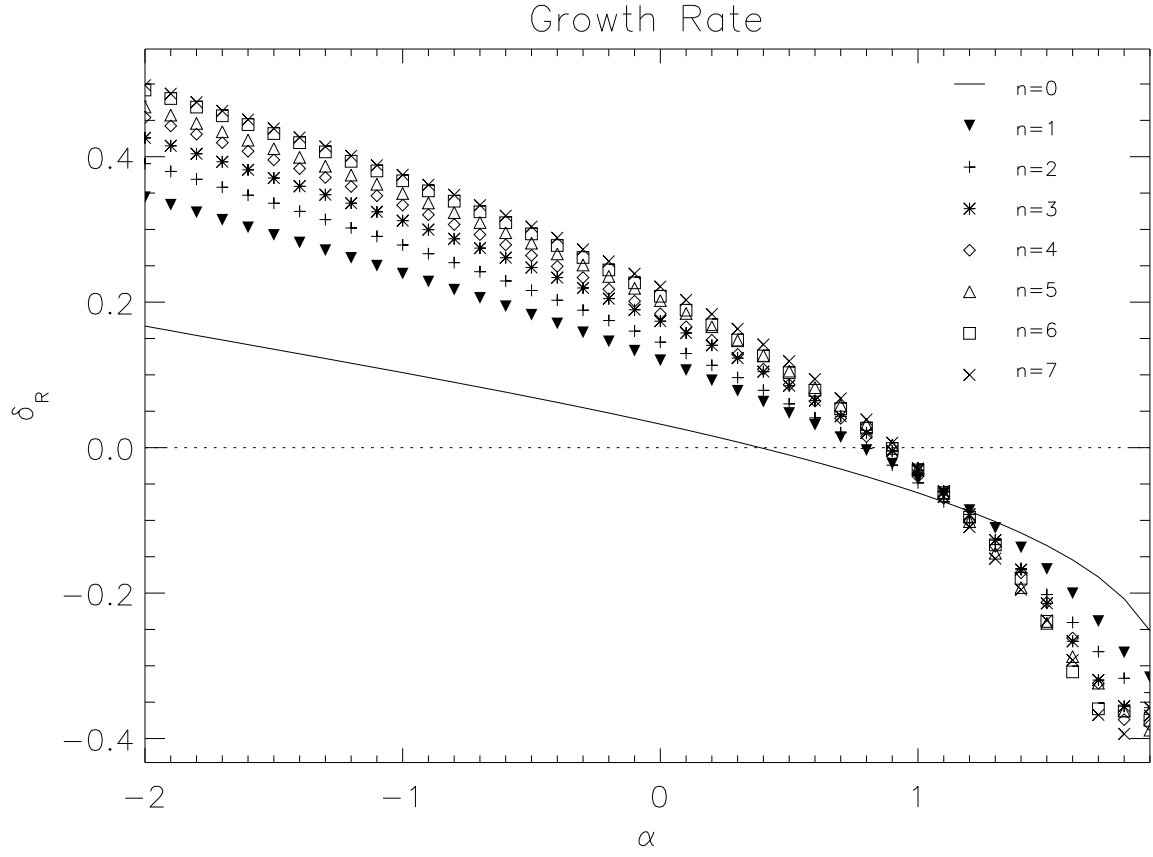


Fig. 2.— Growth/damping rates for the first 8 modes as function of  $\alpha$ . The solid line represents the fundamental mode  $n = 0$ , whereas the different symbols (described by the legend in the upper-right portion of the plot) correspond to the seven overtones  $1 \leq n \leq 7$ . Eigenmodes with  $\delta_R < 0$  are stable, whereas modes with  $\delta_R > 0$  are unstable.

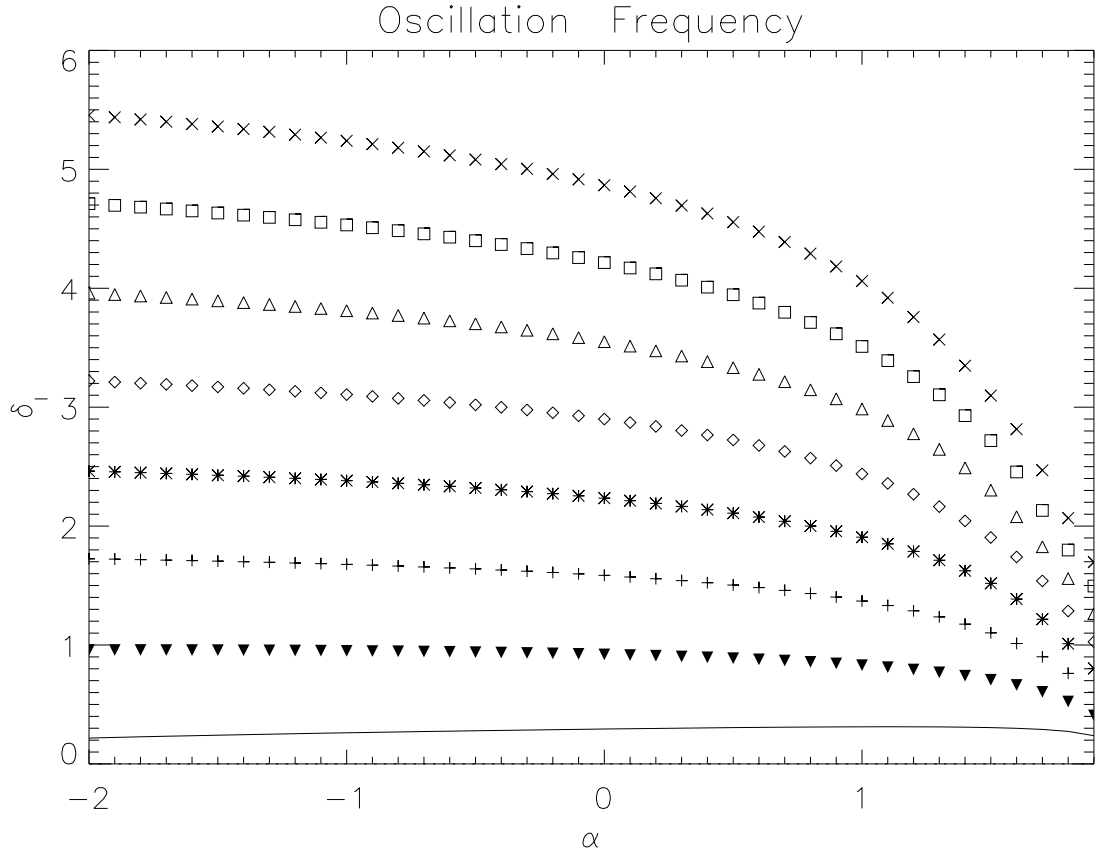


Fig. 3.— Oscillation frequencies for the first 8 modes as function of  $\alpha$ . The symbols have the same meaning as in Figure 2. Modes with  $1 \leq n \leq 7$  have oscillation frequencies that are monotonically decreasing functions of  $\alpha$ . For the fundamental mode ( $n = 0$ ), however,  $\delta_1$  increases to reach a maximum at approximately  $\alpha = 1.1$  and decreases afterwards.

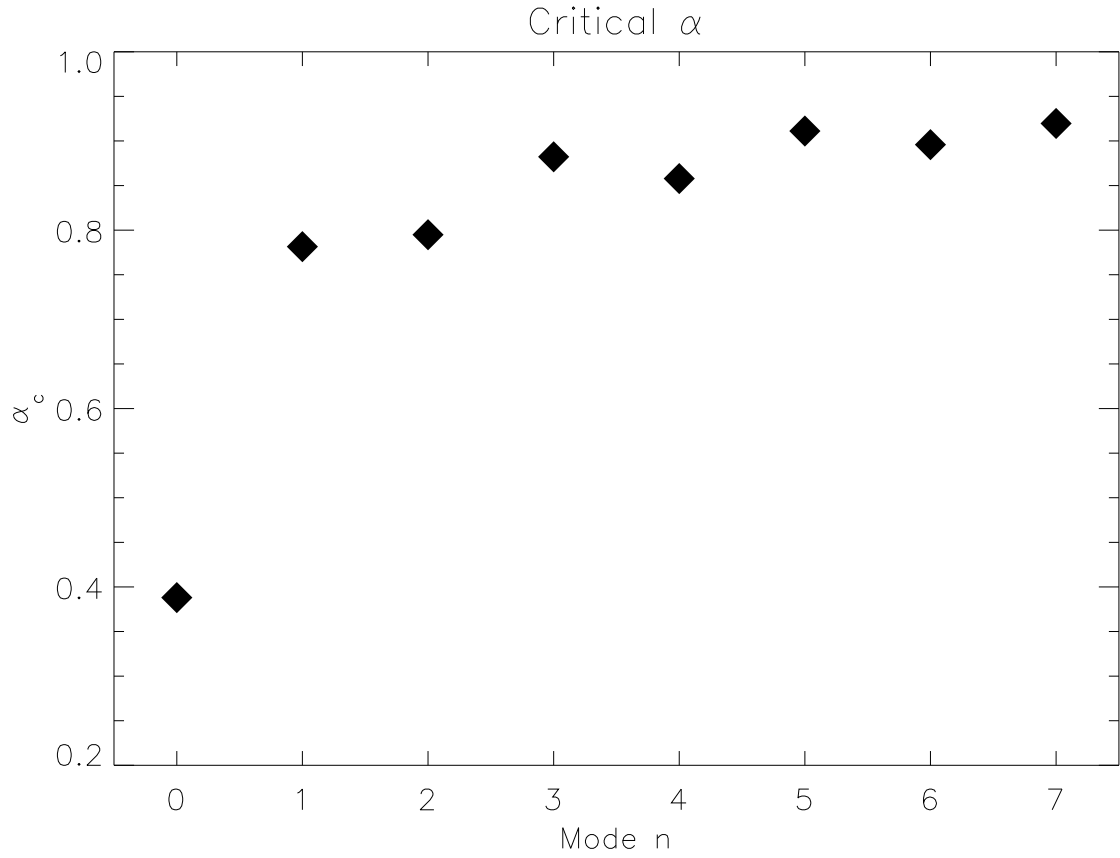


Fig. 4.— Critical value of the cooling index as function of the mode number  $n$ . For a given mode  $n$ , values of  $\alpha > \alpha_c$  have negative growth rates and thus are stable.

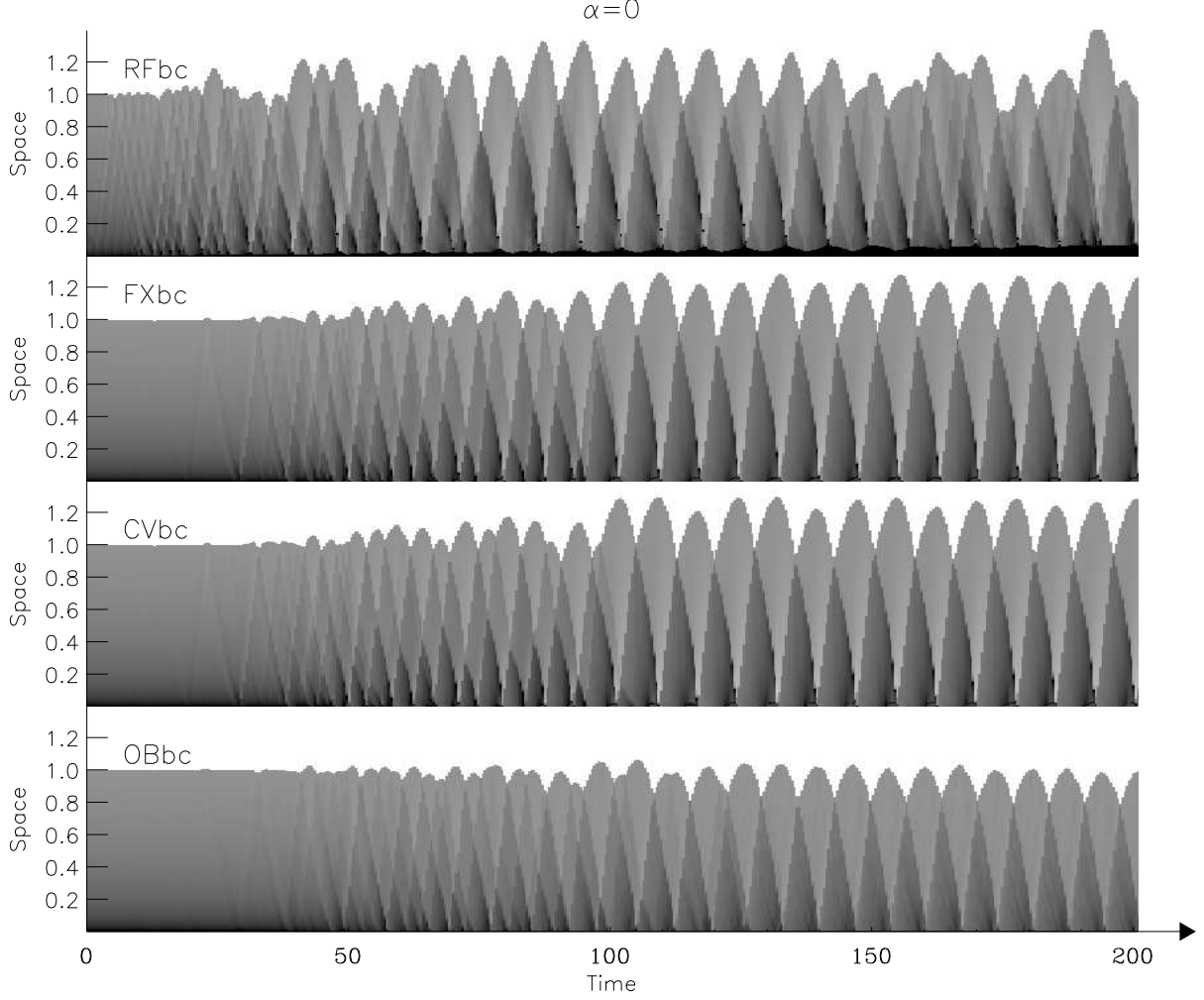


Fig. 5.— Space-time diagrams for  $\alpha = 0$  and the four different boundary conditions described in the text. From top to bottom: the reflective boundary condition (RFbc), the fixed boundary condition (FXbc), the constant velocity boundary condition (CVbc) and the “open boundary” condition (OBbc). The spatial coordinate is represented on the vertical axis, whereas the time evolution of the system is described by the horizontal axis. Time is expressed in units of  $L_c/|v_{in}|$ , where  $L_c$  is the length of the cooling region in steady-state, see §3.1, and  $v_{in}$  is the fluid velocity ahead of the shock. In each panel, the gas flows supersonically from the top to the bottom. The gray-scale shows the density logarithm: lighter (darker) shades corresponds to lower (higher) density regions.



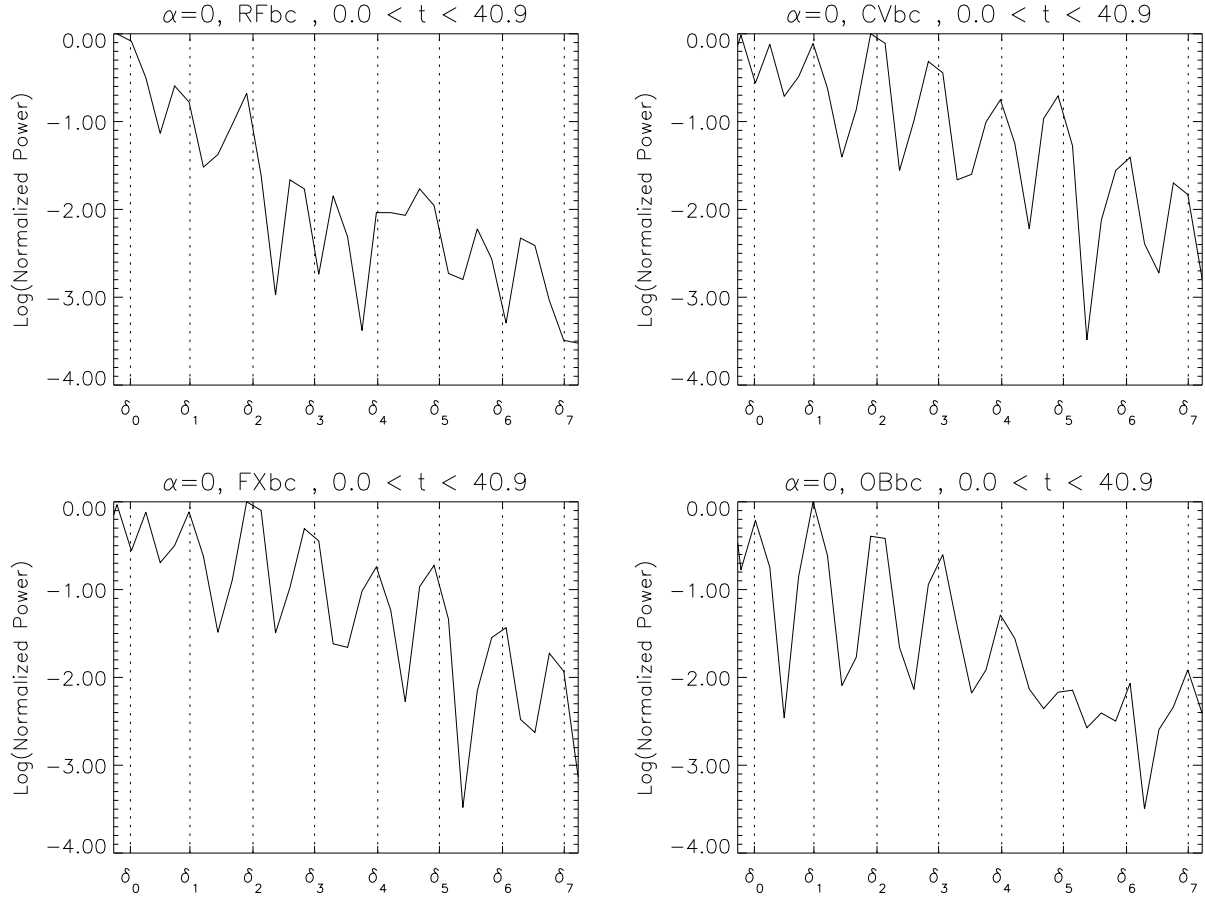


Fig. 6.— Power spectra of the shock position for  $\alpha = 0.0$  derived from the numerical simulations for the four boundary conditions described in the text. On the top: reflective (left) and constant velocity boundary conditions (right); on the bottom: the fixed (left) and open boundary condition (right). The vertical axis represents power on a logarithmic scale, normalized to its maximum value. The horizontal axis shows frequency on a linear scale. The power spectra are obtained by computing the Fourier transform of the function  $x_{\text{sh}}(t) - x_{\text{sh}}(0)$ , where  $x_{\text{sh}}(t)$  is the shock position at time  $t$ . The transform is taken over a sample of length  $0 < t < 40.9$ . The dashed vertical lines in correspondence of the  $\delta_n$ , with  $0 \leq n \leq 7$ , mark the oscillation eigenfrequencies derived from linear analysis, see Table 1.

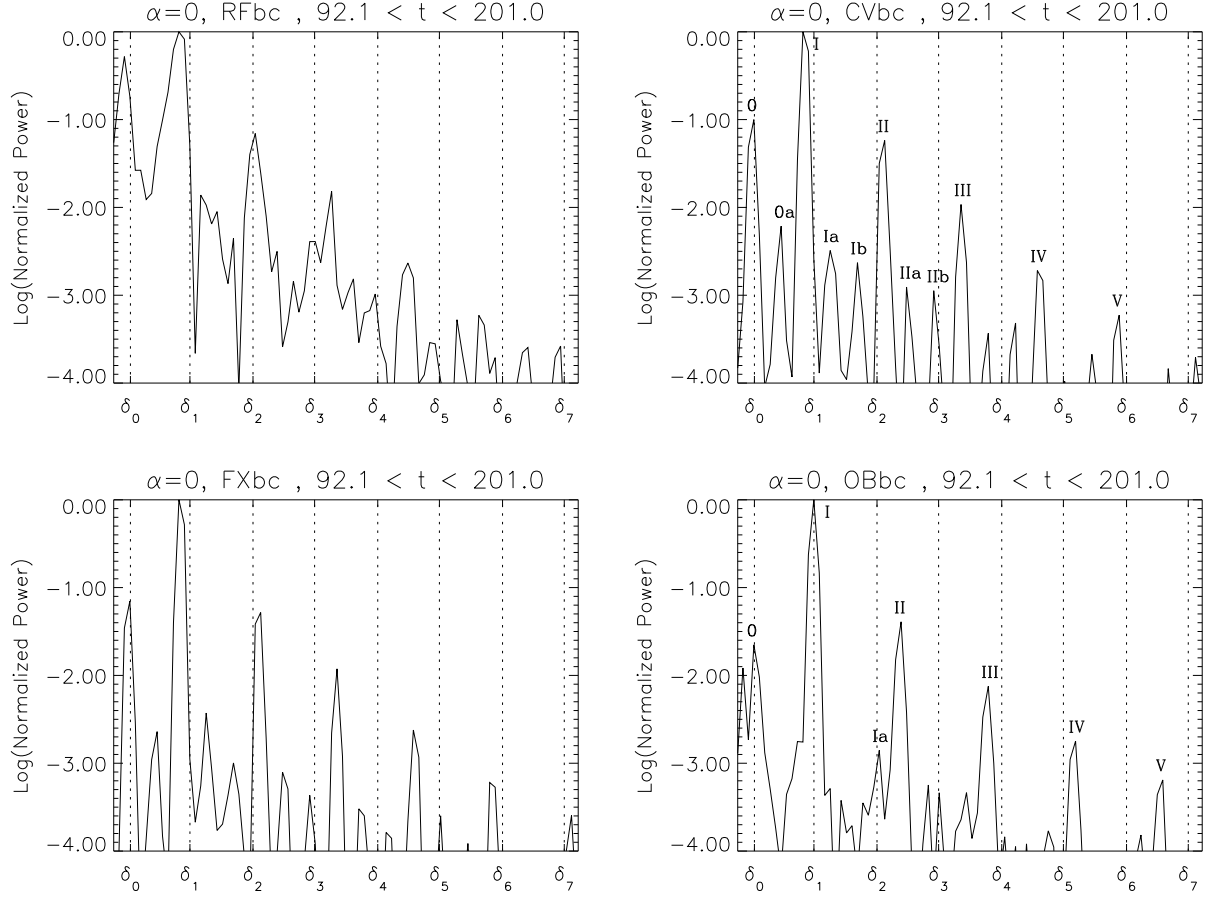


Fig. 7.— Same as Figure 6, but when a longer portion of the shock position at later evolutionary times ( $92.1 < t < 201$ ) is Fourier-transformed. For the CVbc and OBbc, a main sequence of overtones (I, II, III and so forth) with frequencies  $\Omega^{(I)}$ ,  $\Omega^{(II)}$ ,  $\Omega^{(III)}$ ,  $\dots$ , may be identified from the plots. These modes are almost equally spaced in frequency and may result from nonlinear mode-mode coupling between the fundamental mode and the first overtone. Secondary harmonics with oscillation frequencies  $\Omega^{(Ia)}$ ,  $\Omega^{(IIa)}$ ,  $\Omega^{(IIb)}$ , etc., appear between the main sequence modes. The explicit values of the  $\Omega$ 's are given in Table 4.

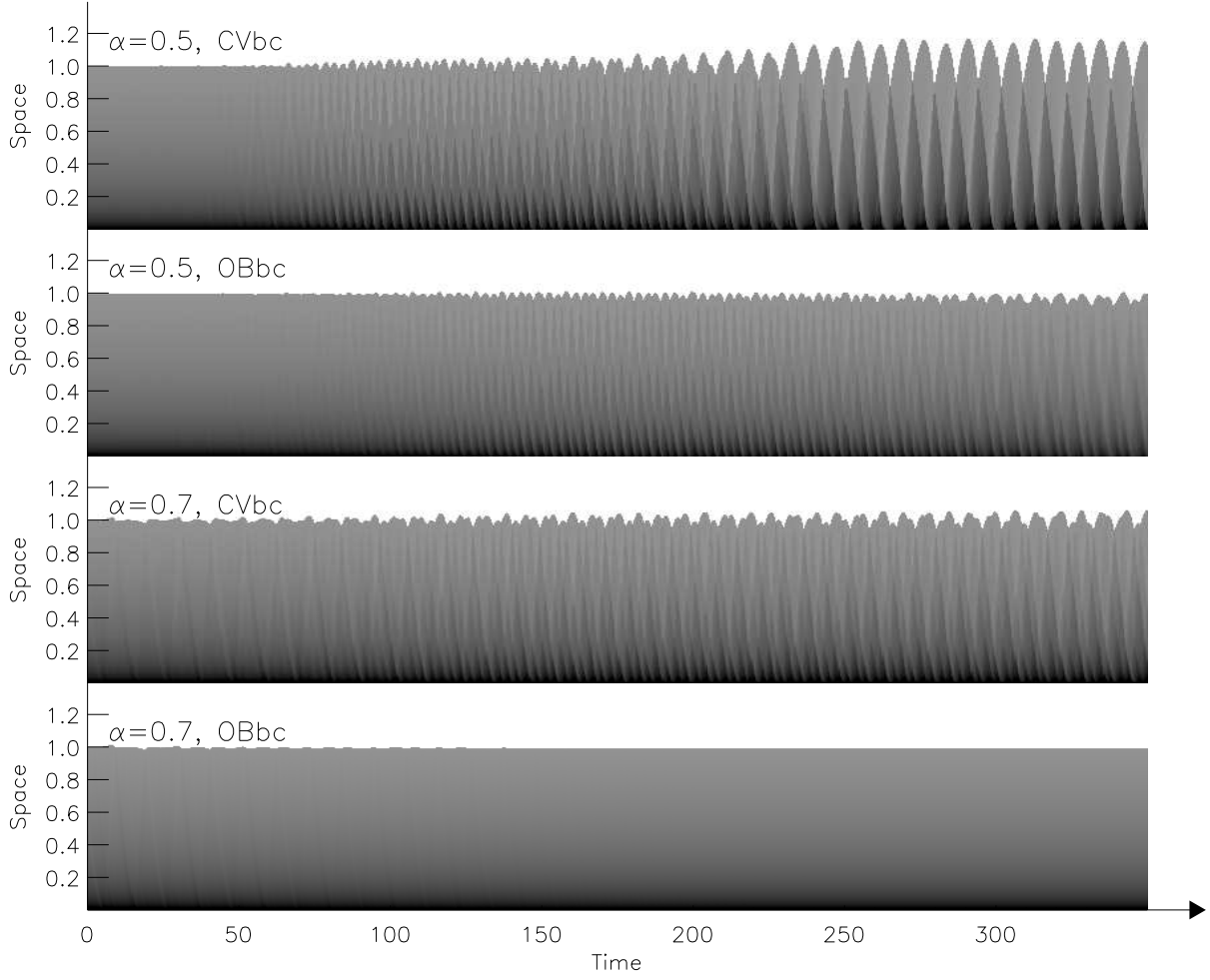


Fig. 8.— Evolutionary space-time diagrams for  $\alpha = 0.5, 0.7$  with the OBbc and CVbc. Oscillation amplitudes are considerably reduced when  $\alpha$  increases and also when the OBbc is adopted. In the worst case (bottom panel), the initial perturbation is damped and the system returns to a stationary, stable configuration.

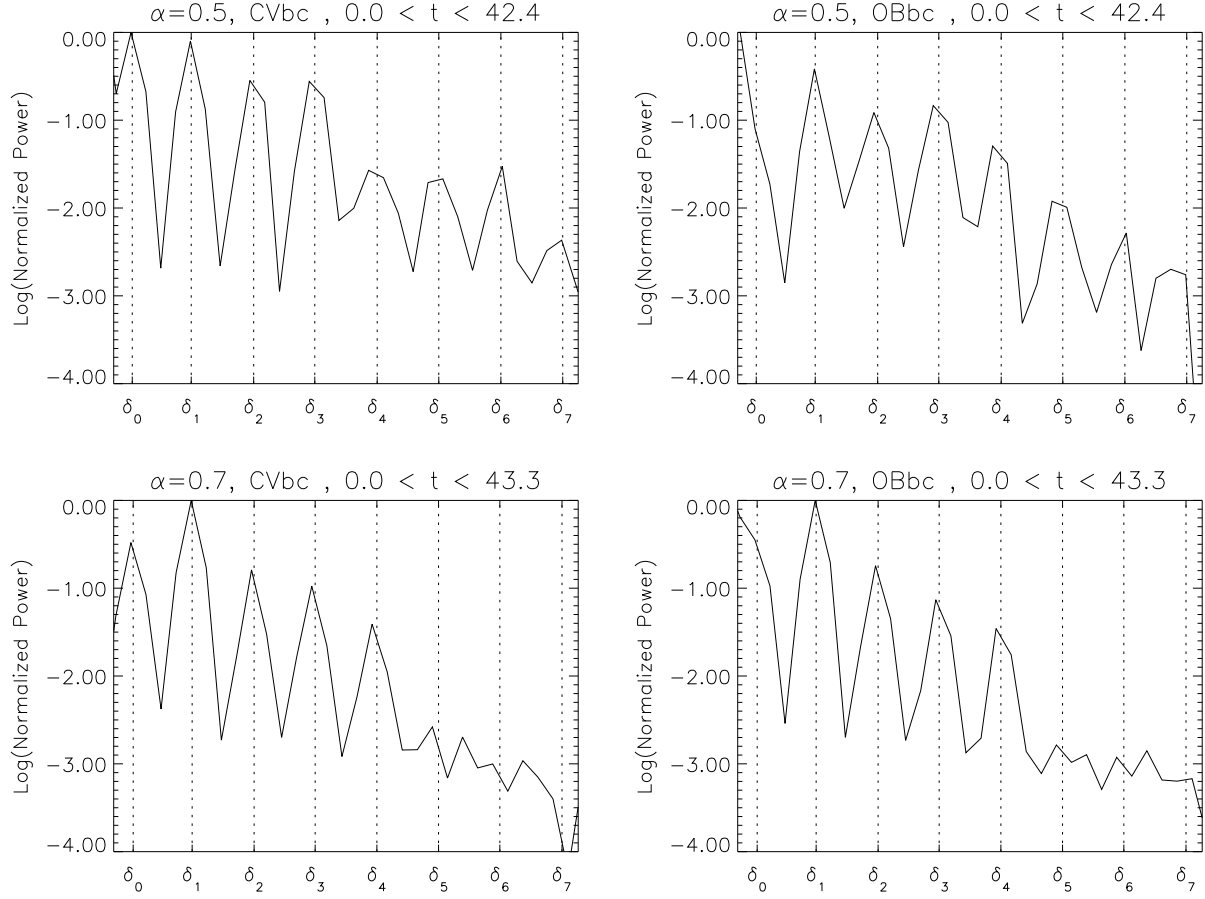


Fig. 9.— Power spectra for  $\alpha = 0.5$  (top) and  $\alpha = 0.7$  (bottom) during the early phases of evolution,  $0 < t < 42.4$  and  $0 < t < 43.3$ , respectively. Results obtained with the constant velocity and open boundary condition are shown on the left and on the right, respectively. The dashed vertical lines correspond to the frequencies derived from linear analysis. The vertical and horizontal axis have the same meaning as in Fig. 6.

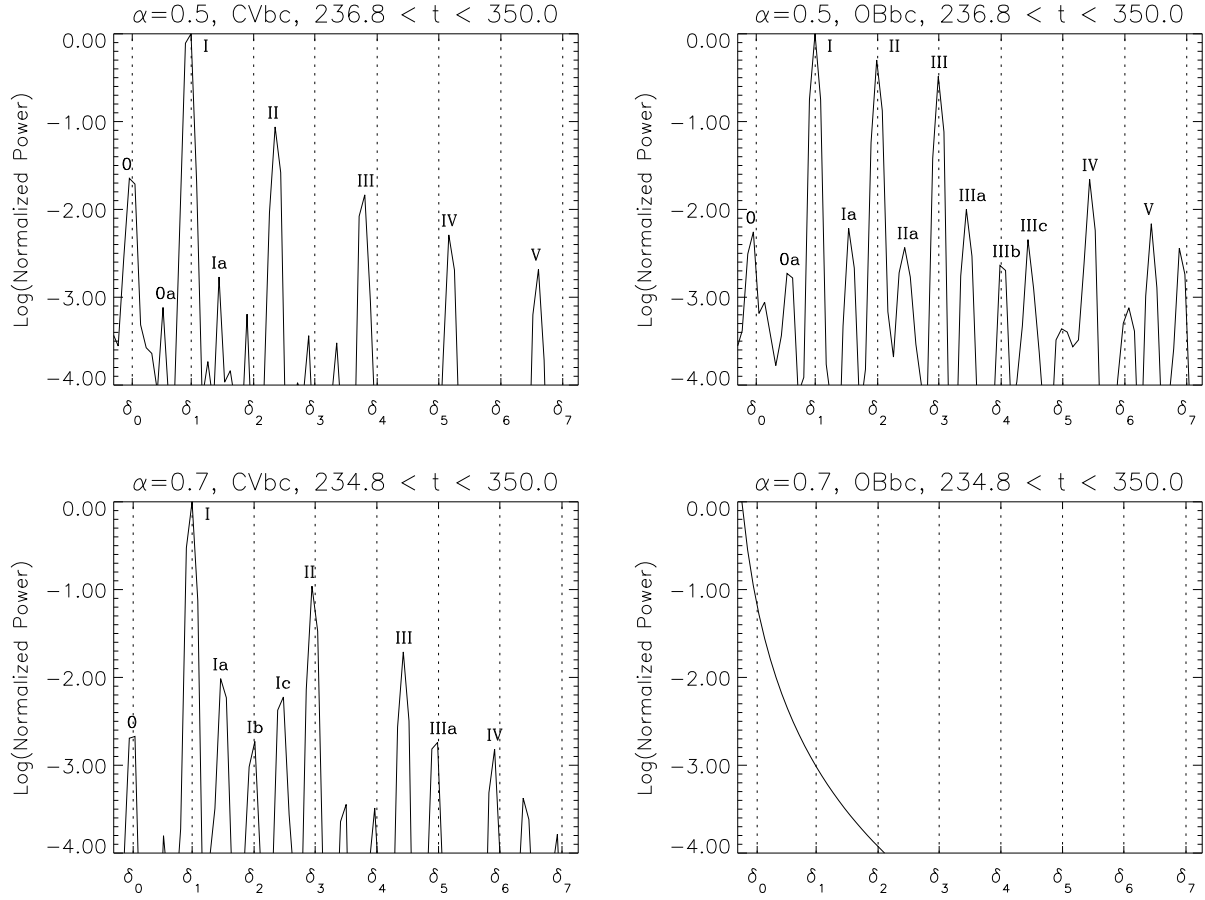


Fig. 10.— Same as Fig. 9, but for a longer portion of the oscillatory cycle during the late evolutionary phases,  $236.8 < t < 350$  (for  $\alpha = 0.5$ ) and  $234.8 < t < 350$  (for  $\alpha = 0.7$ ). During this time window, the oscillation amplitudes have fully saturated and a main sequence of modes, similar to those described in Fig. 7, may be distinguished in the power spectra. The corresponding oscillation frequencies are labeled by  $\Omega^{(I)}$ ,  $\Omega^{(II)}$ ,  $\Omega^{(III)}$ , and so on. A number of secondary harmonics ( $\Omega^{(Ia)}$ ,  $\Omega^{(IIa)}$ ,  $\Omega^{(IIb)}$ , etc.) is present as well. Notice that the fundamental mode  $\Omega^{(0)}$ , although linearly stable, is still present (with little power) in the spectra. Values of the different  $\Omega$ 's are listed in Table 4. When  $\alpha = 0.7$  and the OBbc is used, the system returns to steady-state and a flat spectrum is obtained.

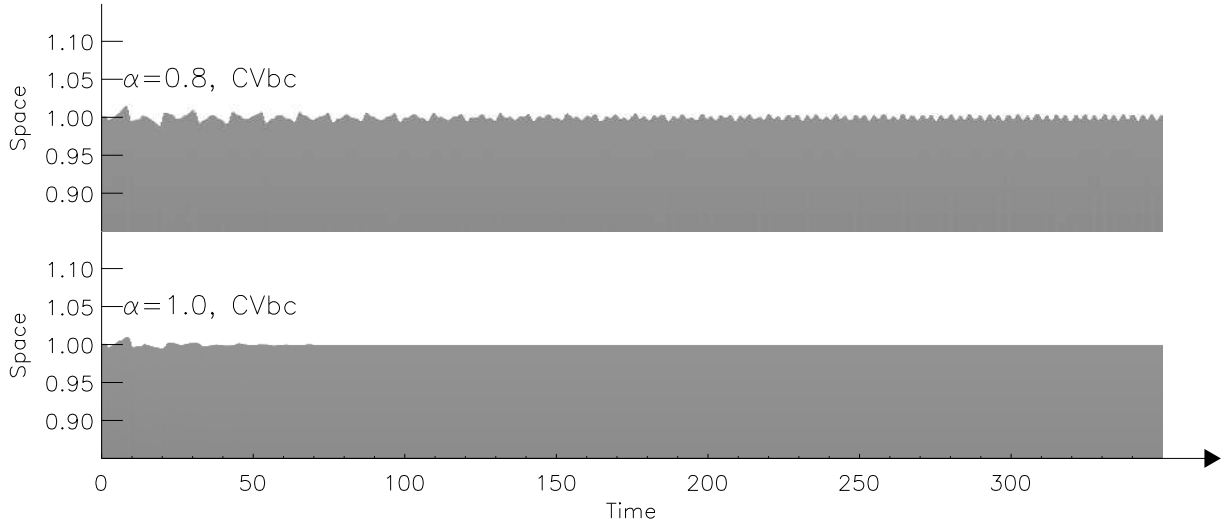


Fig. 11.— Space-time evolutionary diagram for  $\alpha = 0.8$  (on the top) and  $\alpha = 1$  (on the bottom) is shown. Only the CVbc has been employed. In order to make the oscillations more visible, the spatial scale in the plot shows a small area around the shock position.

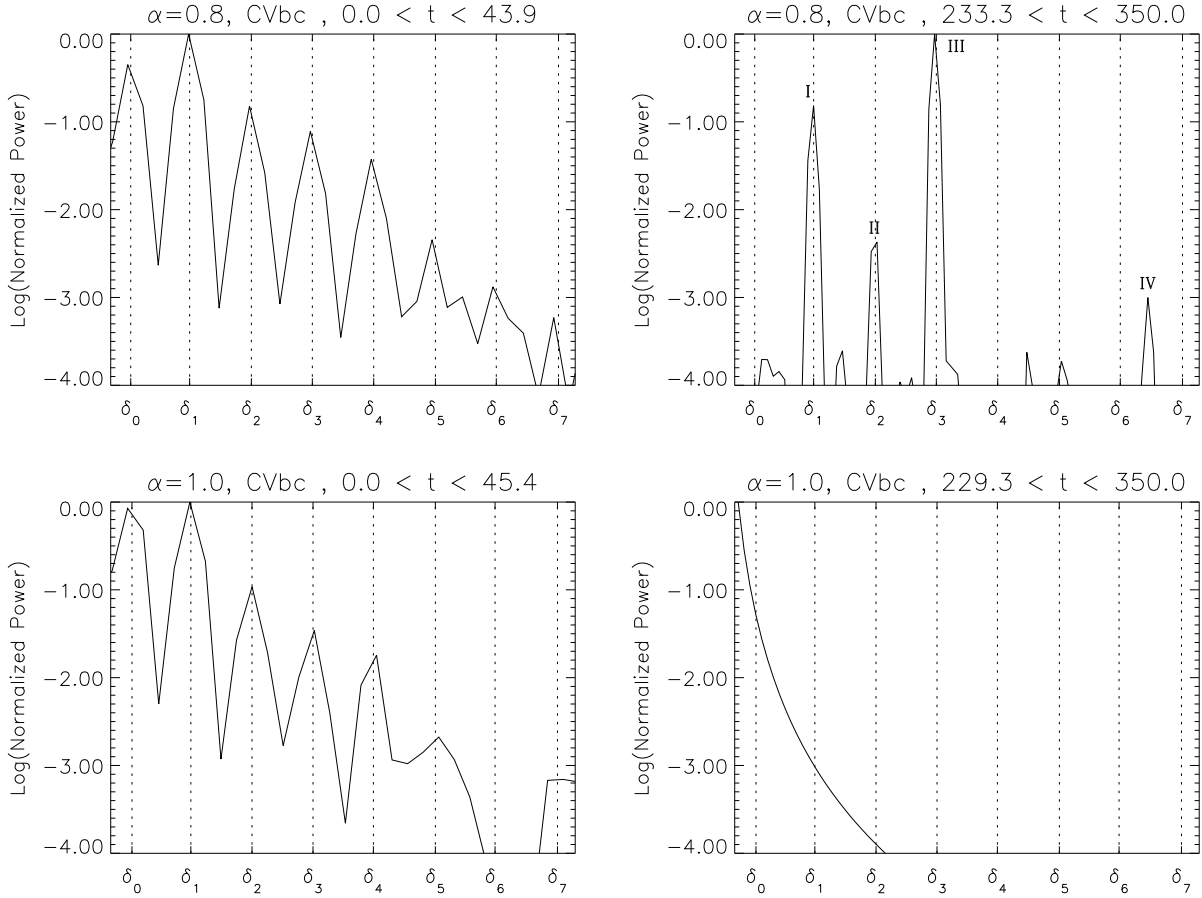


Fig. 12.— Power spectra for  $\alpha = 0.8$  (top panel) and  $\alpha = 1$  (bottom panel). The earlier ( $0 < t < 43.9$  for  $\alpha = 0.8$  and  $0 < t < 45.4$  for  $\alpha = 1$ ) and later ( $233.3 < t < 350$  for  $\alpha = 0.8$  and  $229.3 < t < 350$  for  $\alpha = 1$ ) simulation phases are shown to the left and to the right, respectively. Only the  $\alpha = 0.8$  case evolves into a (weakly) nonlinear phase, characterized by very small-amplitude oscillations. Notice how the first and second harmonics, although linearly stable, are still present during the later simulation phases ( $\Omega^{(I)}$  and  $\Omega^{(II)}$  on the top, right panel). The fundamental mode is practically absent. Explicit values of the nonlinear overtones are given in Table 4. When  $\alpha = 1$ , the initial perturbation produces modes that can be clearly identified with the linear ones (bottom, left panel). These modes are absent during the later phases (bottom, right panel), thus confirming that the shock is stable.

Table 1. Real and imaginary parts of the complex eigenfrequencies  $\delta = \delta_R + i\delta_I$  are given for the first eight modes,  $n = 0..7$ , and for negative values of  $\alpha$ . The lower portion of the Table shows the coefficients derived from the linear fit  $\delta_I^{(n)} = \tilde{\delta}_I^{(0)} + n\Delta\tilde{\delta}_I$ , where  $\tilde{\delta}_I^{(0)}$  is the “fitted” fundamental mode and  $\Delta\tilde{\delta}_I$  is the frequency spacing.

Mode	$\alpha = -2$		$\alpha = -3/2$		$\alpha = -1$		$\alpha = -1/2$	
	$\delta_R$	$\delta_I$	$\delta_R$	$\delta_I$	$\delta_R$	$\delta_I$	$\delta_R$	$\delta_I$
$n = 0$	0.1671	0.2175	0.1353	0.2416	0.1031	0.2616	0.0693	0.2787
$n = 1$	0.3443	0.9581	0.2925	0.9566	0.2393	0.9510	0.1827	0.9399
$n = 2$	0.3905	1.7252	0.3360	1.7052	0.2786	1.6778	0.2161	1.6398
$n = 3$	0.4258	2.4622	0.3707	2.4277	0.3121	2.3820	0.2476	2.3204
$n = 4$	0.4538	3.2200	0.3957	3.1704	0.3334	3.1059	0.2642	3.0197
$n = 5$	0.4684	3.9594	0.4110	3.8945	0.3495	3.8112	0.2812	3.7012
$n = 6$	0.4918	4.7110	0.4319	4.6330	0.3669	4.5325	0.2938	4.3996
$n = 7$	0.4982	5.4548	0.4389	5.3604	0.3749	5.2400	0.3039	5.0819
	$\tilde{\delta}_I^{(0)}$	$\Delta\tilde{\delta}_I$	$\tilde{\delta}_I^{(0)}$	$\Delta\tilde{\delta}_I$	$\tilde{\delta}_I^{(0)}$	$\Delta\tilde{\delta}_I$	$\tilde{\delta}_I^{(0)}$	$\Delta\tilde{\delta}_I$
	0.2183	0.7486	0.2352	0.7324	0.2502	0.7129	0.2642	0.6882

Table 2. Real and imaginary parts of the complex eigenfrequencies  $\delta = \delta_R + i\delta_I$  are given for the first eight modes,  $n = 0..7$ , and for nonnegative values of  $\alpha$ . The rightmost column gives the critical value of  $\alpha$  for a given mode  $n$ , such that for  $\alpha > \alpha_c^{(n)}$  the  $n$ -th mode is stable. The lower portion of the Table lists the coefficients derived from the linear fit.

Mode	$\alpha = 0$		$\alpha = 1/2$		$\alpha = 1$		$\alpha = 3/2$		$\alpha_c$
	$\delta_R$	$\delta_I$	$\delta_R$	$\delta_I$	$\delta_R$	$\delta_I$	$\delta_R$	$\delta_I$	
$n = 0$	0.0323	0.2934	-0.0101	0.3052	-0.0622	0.3121	-0.1346	0.3054	0.3881
$n = 1$	0.1201	0.9210	0.0476	0.8887	-0.0420	0.8307	-0.1668	0.7075	0.7815
$n = 2$	0.1450	1.5857	0.0602	1.5043	-0.0485	1.3698	-0.2020	1.1022	0.7949
$n = 3$	0.1739	2.2347	0.0851	2.1087	-0.0310	1.9068	-0.2141	1.5186	0.8822
$n = 4$	0.1841	2.9003	0.0865	2.7242	-0.0396	2.4386	-0.2128	1.9042	0.8578
$n = 5$	0.2021	3.5505	0.1052	3.3322	-0.0280	2.9850	-0.2416	2.3021	0.9111
$n = 6$	0.2081	4.2158	0.1030	3.9454	-0.0307	3.5106	-0.2390	2.7186	0.8959
$n = 7$	0.2214	4.8666	0.1188	4.5561	-0.0286	4.0605	-0.2375	3.0974	0.9196
	$\tilde{\delta}_I^{(0)}$	$\Delta\tilde{\delta}_I$	$\tilde{\delta}_I^{(0)}$	$\Delta\tilde{\delta}_I$	$\tilde{\delta}_I^{(0)}$	$\Delta\tilde{\delta}_I$	$\tilde{\delta}_I^{(0)}$	$\Delta\tilde{\delta}_I$	
	0.2774	0.6553	0.2898	0.6088	0.3011	0.5359	0.3076	0.3998	



Table 3. Relative errors of the oscillation frequencies found from the numerical simulations during the early linear phases. The errors are computed as  $|\omega_I^{(n)}/\delta^{(n)} - 1|$ , where  $\omega_I^{(n)}$  corresponds to the closest frequency peak referred to the theoretical value. Notice that the finite length of the time window  $\Delta t$  over which the Fourier transform is taken introduces an uncertainty  $\sim 1/\Delta t$ .

	$\alpha = 0$		$\alpha = 1/2$		$\alpha = 0.7$		$\alpha = 0.8$	$\alpha = 1$
Mode	CVbc	OBbc	CVbc	OBbc	CVbc	OBbc	CVbc	CVbc
$n = 0$	0.482	0.036	0.039	-	0.071	-	0.087	0.122
$n = 1$	0.010	0.010	0.008	0.008	0.010	0.010	0.010	0.010
$n = 2$	0.042	0.042	0.025	0.025	0.017	0.017	0.012	0.0003
$n = 3$	0.048	0.020	0.026	0.026	0.016	0.016	0.009	0.006
$n = 4$	0.005	0.005	0.031	0.031	0.017	0.017	0.009	0.011
$n = 5$	0.016	0.027	0.012	0.032	0.018	0.018	0.010	0.010
$n = 6$	0.009	0.009	0.004	0.004	0.018	0.018	0.008	-
$n = 7$	0.032	0.001	0.035	0.035	0.046	0.013	0.010	0.012

Table 4. Nonlinear frequencies relative to the later evolutionary phases for  $\alpha = 0, 0.5, 0.7$  and  $0.8$ . Frequencies labeled with  $\Omega^{(I)}$ ,  $\Omega^{(II)}$ ,  $\Omega^{(III)}$ , and so on, identify the main sequence overtones, whereas the intermediate secondary modes are enumerated by appending a letter to the main sequence mode number that precedes it (i.e.  $\Omega^{(Ia)}$ ,  $\Omega^{(IIa)}$ ,  $\Omega^{(IIb)}$ , etc.) The error introduced by the Fourier transform is  $\sim 1/\Delta t$ , where  $\Delta t$  is the time window over which the transform is taken.

	$\alpha = 0$		$\alpha = 1/2$		$\alpha = 0.7$	$\alpha = 0.8$
Mode	CVbc	OBbc	CVbc	OBbc	CVbc	CVbc
$\Omega^{(0)}$	0.287	0.287	0.278	0.278	0.326	-
$\Omega^{(0a)}$	0.575	-	0.611	0.611	-	-
$\Omega^{(I)}$	0.805	0.920	0.888	0.888	0.869	0.858
$\Omega^{(Ia)}$	1.092	-	1.166	1.222	1.141	-
$\Omega^{(Ib)}$	1.379	-	1.444	-	1.467	-
$\Omega^{(Ic)}$	-	-	-	-	1.738	-
$\Omega^{(II)}$	1.667	1.839	1.721	1.499	2.010	1.448
$\Omega^{(IIa)}$	1.897	-	-	1.777	-	-
$\Omega^{(IIb)}$	2.184	-	-	-	-	-
$\Omega^{(III)}$	2.471	2.759	2.554	2.110	2.879	1.985
$\Omega^{(IIIa)}$	2.759	-	-	2.388	3.205	-
$\Omega^{(IIIb)}$	3.046	-	-	2.721	-	-
$\Omega^{(IIIc)}$	-	-	-	2.999	-	-
$\Omega^{(IV)}$	3.276	3.678	3.443	3.609	3.748	3.969
$\Omega^{(V)}$	4.138	4.598	4.331	4.220	-	-